Development of a Clear-Sky 3D Sub-Grid Terrain Solar Radiative Effect Parameterization Scheme Based on the Mountain Radiation Theory

Anning Huang[1] [ORCID], **Chunlei Gu[1], Yaocun Zhang[1]** [ORCID]**, Weiping Li[2,3], Lujun Zhang[1], Yang Wu[1], Xindan Zhang[1], and Shuxin Cai[1]**

[1]CMA-NJU Joint Laboratory for Climate Prediction Studies and State Key Laboratory of Severe Weather and Joint Center for Atmospheric Radar Research of CMA/NJU, School of Atmospheric Sciences, Nanjing University, Nanjing, China, [2]CMA Earth System Modeling and Prediction Centre (CEMC), China Meteorological Administration (CMA), Beijing, China, [3]State Key Laboratory of Severe Weather (LaSW), China Meteorological Administration (CMA), Beijing, China

Abstract Terrains strongly affect the surface solar radiation (SSR) and energy balance, and further greatly modulate the weather and climate in rugged areas. In this study, we have developed a clear-sky 3-dimensional sub-grid terrain solar radiative effect (3DSTSRE) parameterization scheme based on the mountain radiation theory with full consideration of the influences of 3-dimensional configuration of terrains. Results show that the 3DSTSRE scheme achieves the equivalent effect of the downward SSR flux at the model grids derived from those explicitly calculated at the sub-grids without reducing the calculating efficiency of numerical models. It performs well at model grids with different horizontal resolutions. The instant downward SSR flux calculated by the 3DSTSRE scheme at 76.8%, 84.8%, 88.7%, 91.6%, 93.0%, and 87.1% model grids with the horizontal resolution of 0.025°, 0.05°, 0.1°, 0.2°, 0.4°, and 0.8° in the areas featured by complex terrains shows relative errors within $\pm 1.0\%$ against those derived from the explicit calculations at sub-grids, respectively. The normalized mean absolute errors of the instant downward SSR flux calculated by the 3DSTSRE scheme are below 1% (2%) throughout the day and the year for the model grids with resolutions ranging from 0.05° to 0.8° (of 0.025°). Although the performance of 3DSTSRE scheme decreases slightly under the conditions with much lower solar zenith angle and finer model horizontal resolution, the 3DSTSRE scheme developed in current study shows broad application prospects in various numerical models with the advantages of a solid physical foundation, high accuracy, strong portability and flexibility.

1. Introduction

Terrains with different scales significantly affect the weather and climate by regulating the atmospheric circulation through dynamic and thermal effects (Sandu et al., 2019; Wu et al., 2017). Effective representation of complex terrain and related effects has long been a difficult problem in numerical simulation studies (Davies & Brown, 2001; Jiménez & Dudhia, 2012; Phillips, 1957; Wallace et al., 1983; Xu et al., 2019). Adopting high-resolution grid-scale topography improves the model performance (Hua et al., 2020; Ji & Kang, 2013). However, the models perform worse when increasing the resolution to a certain degree without correspondingly improving the description of physical process (Carvalho et al., 2012; Falasca & Curci, 2018; Mass et al., 2002; Maurya et al., 2018), especially the sub-grid terrain related processes (Elvidge et al., 2019; Lalande et al., 2021; Yu et al., 2019).

State-of-art meteorological models with high horizontal resolutions still have difficulties in reproducing the mountain climate and weather well. For example, large cold-wet biases over the Tibetan Plateau are common in numerical models (Li et al., 2021; Niu et al., 2021; Zhu & Yang, 2020). The dynamic effects of sub-grid terrain, such as orographic drags, have gained wide attention and become well parameterized (van Niekerk et al., 2020; Vosper et al., 2020; Wang et al., 2020). Better representations of the sub-grid terrain thermal effects are also vital to the model performance (Zhou et al., 2019). However, the computationally economical and physically reliable schemes of sub-grid thermal effects, such as sub-grid terrain solar radiative effect (STSRE), are still scarce.

The STSRE strongly influences the land surface energy exchange and thereafter weather and climate at local to regional scales (Barry, 2008; Wang et al., 2002). The importance of the STSRE in numerical models has been recognized along with the continuous increase in model horizontal resolution (Feng & Zhang, 2007; Gu

Writing – original draft: Anning Huang, Chunlei Gu
Writing – review & editing: Anning Huang, Yaocun Zhang, Weiping Li, Lujun Zhang, Yang Wu, Xindan Zhang, Shuxin Cai

et al., 2012). Three kinds of STSRE schemes have been applied to numerical models, namely the 2-dimensional (2D) STSRE scheme based on Kondrat'yev (1965), the Monte Carlo scheme based on the Monte Carlo photon tracking technology (Chen et al., 2006; Liou et al., 2007), and the 3-dimensional (3D) STSRE scheme based on the mountain radiation theory consider the synergetic influences of the self and surrounding terrains (Dozier & Frew, 1990; Dubayah, 1994). These schemes greatly improve the model performance in estimating the land surface energy exchanges, temperature, atmospheric circulations, and even precipitation (Hao et al., 2021; Lee et al., 2013, 2015, 2019; Manners et al., 2012; Müller & Scherer, 2005; Shen & Hu, 2006; Zhang et al., 2006). However, they have their own limitations. The 2D STSRE schemes neglect the radiative impacts of the surrounding terrains (Olyphant, 1984). Uncertainties remain in the Monte Carlo scheme because (a) the photon tracking results are not evaluated by the observations, and (b) the parameterized function regression coefficients vary discontinuously under different solar elevation angles and albedo (see Tables 1, 3, and 4 in Lee et al., 2011).

The type of 3-dimensional sub-grid terrain solar radiative effect (3DSTSRE) schemes has a solid physical foundation and agrees well with observations (Ruiz-Arias et al., 2010; Tovar-Pescador et al., 2006). However, the large calculation amount of 3DSTSRE schemes limited their applications in numerical models. Most studies only consider the radiative effect of 2D topographical configuration in models (Gu et al., 2020; Han et al., 2018; He et al., 2019; Huang & Qian, 2008), leading to noticeable overestimation of downward surface solar radiation (SSR) flux in mountainous area (Arthur et al., 2018; Hauge & Hole, 2003). Besides, to avoid the complex integration calculations of the 3DSTSRE schemes due to the variation of solar elevation and azimuth, some researchers tended to find empirical statistical relationships between the sky view/shadow factors and terrain slope (Essery & Marks, 2007; Helbig & Lowe, 2012). However, the applicability of these schemes in the area other than their test sites is questionable.

In addition, the elevation data with coarse horizontal resolution (i.e., 10′, 5′, or 1 km) used in the previous studies poorly represent the terrain and STSRE (Liou et al., 2013; Zhang et al., 2002, 2006). Currently, global digital elevation model (DEM) data with resolutions of tens of meters provides valuable opportunities to better describe the detailed 3D configuration of terrain (such as ASTER Global DEM data of Fujisada et al., 2012; TanDEM-X data of Krieger et al., 2007; SRTM DEM data of Jarvis et al., 2008; and ALOS World 3D-30 m data of Takaku et al., 2014).

The 3DSTSRE scheme based on the mountain radiation theory can be easily used to explicitly calculate the downward SSR flux with the high-resolution DEM data. However, the horizontal resolution of most current models ranges from several kilometers to hundreds of kilometers, while the resolution of DEM data is tens of meters, resulting in large discrepancy in the horizontal resolution between the DEM data and models. For the reasons mentioned above, an efficient upscaling method or parameterization scheme should be developed to convert the explicit calculations of downward SSR flux at sub-grid scale (DEM data resolution) into the grid scale (model resolution) to fully consider the impact of 3D terrain configuration on the downward SSR flux in numerical models. We presented a preliminary version of clear-sky 3DSTSRE scheme (Zhang et al., 2022), however, it still has problems of overestimating the terrain shadow effect and neglecting the effect of rugged surface area change on the fluxes. Also, the sensitivity of the scheme's performance to the model resolution remains unclear. These problems demand prompt solution. The aim of this study is to fix these problems and build up a robust clear-sky 3DSTSRE parameterization scheme based on the mountain radiation theory and the DEM data of much finer horizontal resolution with the advantages of a solid physical foundation, high accuracy, minimal computational expense, strong portability and flexibility to the numerical models with different horizontal resolutions.

2. Methodology, Data, Experimental Design, and Evaluation Metrics

2.1. Explicit Calculation Method of Downward SSR Over Rugged Terrain

The downward SSR flux in a plane surface ($E_\downarrow$) includes the direct solar radiation flux ($E_{\text{dir}\downarrow}$) and the diffuse solar radiation flux ($E_{\text{dif}\downarrow}$):

$$E_{\text{dir}\downarrow} = \max\left(E_{\text{ac}} \cdot \left(\frac{r_0}{r}\right)^2 \cdot \tau_b \cdot \cos Z, 0.0\right) \tag{1}$$

$$E_{\text{dif}\downarrow} = \max\left(E_{\text{ac}} \cdot \left(\frac{r_0}{r}\right)^2 \cdot \tau_d \cdot \cos Z, 0.0\right) \tag{2}$$
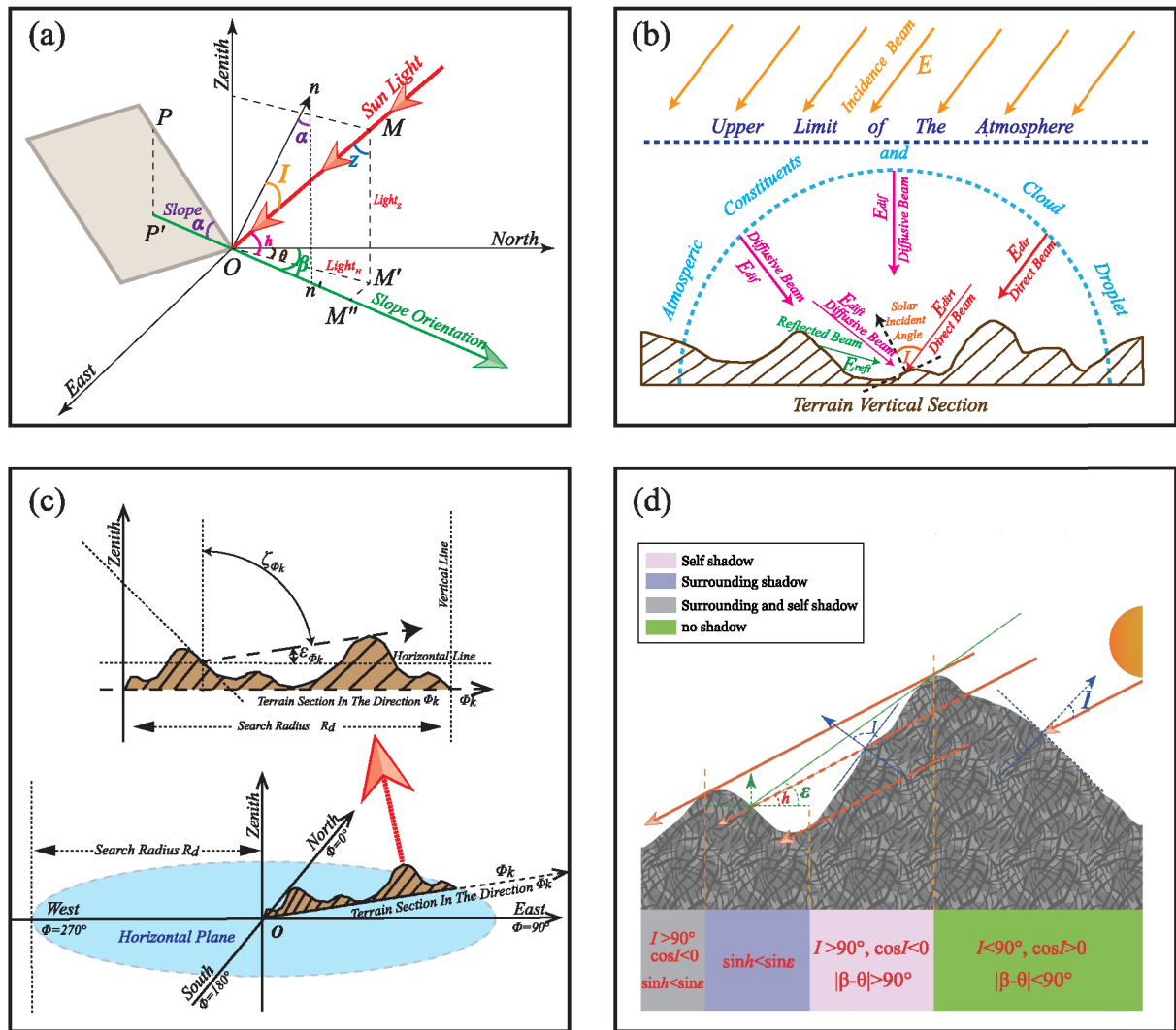
Figure 1. (a) Coordinate of the terrain slope α and aspect β, solar zenith angle Z and elevation angle h, solar azimuth angle θ, and solar incidence angle I on the inclined plane; (b) downward solar radiation components over the areas with complex terrains; (c) the sky view factor and shadow factor; (d) terrain self shadow and cast shadow of the surrounding terrains.

E_{ac}, $(r_0/r)^2$, Z, τ_b, and τ_d are the solar constant, the earth-solar distance factor, the solar zenith angle, and the atmospheric transmittance of $E_{dir\downarrow}$ and $E_{dif\downarrow}$, respectively. As shown in Figure 1a, the solar zenith angle (Z) is the complementary angle of the solar elevation angle (h). h is the acute angle between the horizontal plane and the incident sunlight. Z is calculated by $\cos Z = \sin\varphi\sin\delta + \cos\varphi\cos\delta\cos\omega$. The variables φ, δ, and ω are the latitude, solar declination, and hour angle. $\left(\frac{r_0}{r}\right)^2$, δ, ω, τ_b, and τ_d are calculated following Liu and Jordan (1960), Li and Luo (2015), Kalogirou (2014), Keith and Kreider (1978), and Vician et al. (2017) with respectively.

As shown in Figure 1b, the downward SSR flux $E_{t\downarrow}$ in the rugged surface includes 3 parts, namely, the direct solar radiation flux $E_{dirt\downarrow}$, the diffuse solar radiation flux $E_{dift\downarrow}$, and the solar radiation flux reflected by the surrounding terrains $E_{reft\downarrow}$. The downward SSR components are calculated following Dozier and Frew (1990) and Li et al. (2002):

$$E_{dirt\downarrow} = \max\left(E_{ac}\cdot\left(\frac{r_0}{r}\right)^2\cdot\tau_b\cdot\mathrm{SF}\cdot\cos I, 0.0\right) = \max\left(\mathrm{SF}\cdot E_{dir\downarrow}\cdot\frac{\cos I}{\cos Z}, 0.0\right) \tag{3}$$
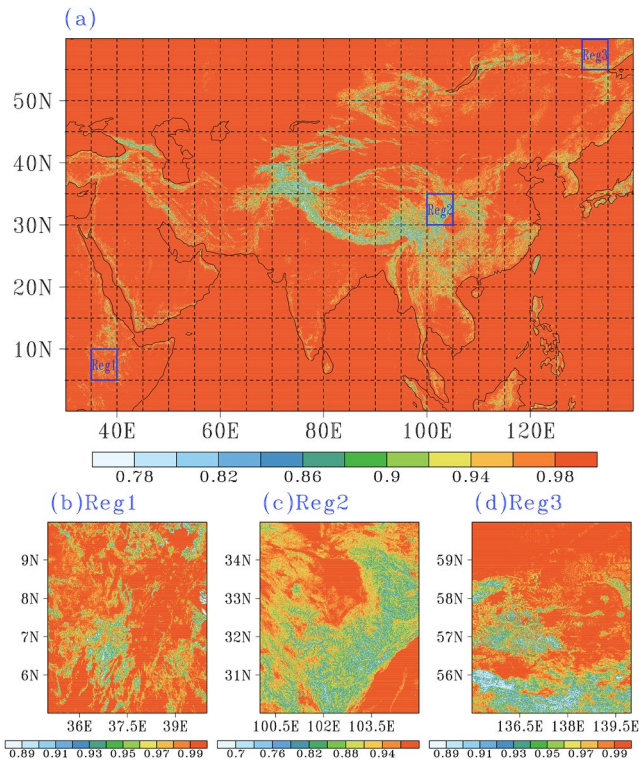
Figure 2. The sky view factor over parts of (a) Eurasia and Africa, (b) Reg1, (c) Reg2, and (d) Reg3 with the grid resolution of 3″ (~90m).

$$E_{\text{dif}\downarrow} = \begin{cases} E_{\text{dif}\downarrow}\left[\dfrac{E_{\text{dirt}\downarrow}}{E_{\text{ac}}} + \dfrac{1}{2}\text{SVF}(1+\cos\alpha)\left(1 - \dfrac{E_{\text{dir}\downarrow}}{E_{\text{ac}}}\right)\right], & \text{if } \cos I > 0 \\ E_{\text{dif}\downarrow}\dfrac{1}{2}\text{SVF}(1+\cos\alpha)\left(1 - \dfrac{E_{\text{dir}\downarrow}}{E_{\text{ac}}}\right), & \text{otherwise} \end{cases} \tag{4}$$

$$E_{\text{reft}\downarrow} = a\left(E_{\text{dir}\downarrow} + E_{\text{dif}\downarrow}\right)\left(\dfrac{1+\cos\alpha}{2} - \text{SVF}\right) \tag{5}$$

The variables a, I, α, SF, and SVF are the surface albedo, sunlight incidence angle, slope, shadow factor, and sky view factor. The albedo a is derived from the MODIS data (MCD43A3) with a resolution of 500 m. I is the angle between the normal of the inclined plane $(\overrightarrow{On})$ and the incident sunlight $(\overrightarrow{OM})$ (Figure 1a). According to Zhang et al. (2006),

$$\cos I = \cos\alpha \cdot \cos Z + \sin\alpha \cdot \sin Z \cdot \cos(\beta - \theta) \tag{6}$$

where β and θ are the terrain aspect and solar azimuth angle. As shown in Figure 1a, α is the angle between the inclined plane and the horizontal plane. α varies from 0° to 90° and represents the steepness of the inclined plane. β is the angle between the normal of the inclined plane projected on the horizontal plane $(\overrightarrow{On'})$ and the north direction. The solar azimuth angle θ is the angle between the projection of the incident sunlight on the horizontal plane $(\overrightarrow{OM'})$ and the north direction. Both β and θ vary from 0° to 360° clockwise. β (θ) in the directions of north, east, south, and west are 0°, 90°, 180°, and 270°, respectively (Figure 1c).

The slope α and aspect β are calculated by the horizontal gradient of the elevation $\left(\dfrac{\partial H}{\partial x} \text{ and } \dfrac{\partial H}{\partial y}\right)$. According to Sharpnack and Akin (1969) and Skidmore (1989),

$$\alpha = \arctan\sqrt{\left(\dfrac{\partial H}{\partial x}\right)^2 + \left(\dfrac{\partial H}{\partial y}\right)^2} \tag{7}$$

$$\beta = \begin{cases} \dfrac{3\pi}{2} - \arctan\left(\dfrac{\partial H}{\partial y}\Big/\dfrac{\partial H}{\partial x}\right), & if \; \dfrac{\partial H}{\partial x} > 0 \\ \dfrac{\pi}{2} - \arctan\left(\dfrac{\partial H}{\partial y}\Big/\dfrac{\partial H}{\partial x}\right), & if \; \dfrac{\partial H}{\partial x} < 0 \\ 0, \; if \; \dfrac{\partial H}{\partial x} = 0 \; \dfrac{\partial H}{\partial y} < 0 \\ \pi, \; if \; \dfrac{\partial H}{\partial x} = 0 \; \dfrac{\partial H}{\partial y} > 0 \\ \text{undefined}, if \; \dfrac{\partial H}{\partial x} = 0 \; \dfrac{\partial H}{\partial y} = 0 \end{cases} \tag{8}$$

$$\text{where} \begin{cases} \dfrac{\partial H}{\partial x} = \dfrac{(H_{i+1,j+1} - H_{i-1,j+1}) + (H_{i+1,j} - H_{i-1,j}) + (H_{i+1,j-1} - H_{i-1,j-1})}{6dx} \\ \dfrac{\partial H}{\partial y} = \dfrac{(H_{i+1,j+1} - H_{i+1,j-1}) + (H_{i,j+1} - H_{i,j-1}) + (H_{i-1,j+1} - H_{i-1,j-1})}{6dy} \end{cases}, i \, (j) \text{ is the grid number along the}$$

x (y) axis.

The solar azimuth angle θ is calculated following Kittler and Darula (2013):

$$\theta = \begin{cases} \pi & \text{if } \cos Z = 1 \\ \arccos\left(\dfrac{\sin\delta - \cos Z \cdot \sin\varphi}{\cos\varphi\sqrt{1 - (\cos Z)^2}} \right) & \text{if } \omega < 0 \text{ and } \cos Z \neq 1 \\ 2\pi - \arccos\left(\dfrac{\sin\delta - \cos Z \cdot \sin\varphi}{\cos\varphi\sqrt{1 - (\cos Z)^2}} \right) & \text{if } \omega > 0 \text{ and } \cos Z \neq 1 \end{cases} \quad (9)$$

The sky view factor SVF (Figure 2) represents the terrain openness and is calculated following Dozier and Frew (1990):

$$\text{SVF} = \frac{1}{N} \sum_{k=1}^{N} \left[\cos\alpha \cdot \cos^2\varepsilon_{\phi_k} + \sin\alpha \cdot \cos(\phi_k - \beta)\left(\frac{\pi}{2} - \varepsilon_{\phi_k} - \sin\varepsilon_{\phi_k} \cdot \cos\varepsilon_{\phi_k} \right) \right] \quad (10)$$

As shown in Figure 1c, ϕ_k is the azimuth angle at the k th direction. ε_{ϕ_k} is the maximal topographic elevation angle in the direction of azimuth angle ϕ_k. It is the angle between the connection line from the adjacent point with the maximum shadow effect to the target point and the horizontal line at the target point in the direction of azimuth angle ϕ_k. N is the total number of the azimuth directions divided.

The shadow factor SF is determined by the solar elevation angle h and the maximal topographic elevation angle ε_{ϕ_k} in the solar azimuth direction ϕ_k at a given time or solar elevation angle h (Figure 1c) according to Dozier and Frew (1990):

$$\text{SF} = \begin{cases} 0 & \text{if } \sin\varepsilon_{\phi_k} > \sin h \\ 1 & \text{if } \sin\varepsilon_{\phi_k} \leq \sin h \end{cases} \quad (11)$$

Much more accuracy of calculated SVF and SF corresponds to more directions divided and larger searching radius, but it will increase the calculation amount. In current study we set the searching radius of 27 km ($\sim$300 sub-grids with the resolution of 3″) and 360 azimuth directions ($N = 360$ in Equation 10) with a resolution of 1°.

In addition, the surface area of the rugged terrain is larger than the area of the horizontal plane. The areas of the sub-grids are different from each other because of the terrain undulation, which influences the solar energy received by the sub-grids. Following Zhang et al. (2006), the grid-scale flux at a model grid p can be explicitly calculated by $\text{flux}_p = \frac{1}{n}\sum_{i=1}^{i=n} \text{flux}_i \cdot \sec\alpha_i / \frac{1}{n}\sum_{i=1}^{i=n} \sec\alpha_i$. The subscripts p and i represent the pth model grid and the i th sub-grid within the model grid p. n is the total number of sub-grids within the model grid p. Considering the area changes of each sub-grid, the grid-scale downward SSR components are derived from the explicit calculations at sub-grids by:

$$E_{\text{dirt},p\downarrow} = \frac{1}{n}\sum_{i=1}^{i=n} \max\left(\cos I_i \cdot \sec\alpha_i \cdot SF_i \cdot \tau_{b_i} \cdot E_{ac}\left(\frac{r_0}{r} \right)^2, 0.0 \right) \bigg/ \frac{1}{n}\sum_{i=1}^{i=n} \sec\alpha_i \quad (12)$$

$$E_{\text{dift},p\downarrow} = \frac{1}{n}\sum_{i=1}^{i=n} \begin{cases} \sec\alpha_i \cdot E_{\text{dif},i\downarrow}\left[\dfrac{E_{\text{dirt},i\downarrow}}{E_{ac}} + \dfrac{1}{2}\text{SVF}_i(1 + \cos\alpha_i)\left(1 - \dfrac{E_{\text{dir},i\downarrow}}{E_{ac}} \right) \right], & \text{if } \cos I_i > 0 \\ \sec\alpha_i \cdot E_{\text{dif},i\downarrow} \cdot \dfrac{1}{2}\text{SVF}_i(1 + \cos\alpha_i)\left(1 - \dfrac{E_{\text{dir},i\downarrow}}{E_{ac}} \right), & \text{otherwise} \end{cases} \bigg/ \frac{1}{n}\sum_{i=1}^{i=n} \sec\alpha_i \quad (13)$$

$$E_{\text{reft},p\downarrow} = \frac{1}{n}\sum_{i=1}^{i=n} a_i \cdot \sec\alpha_i(E_{\text{dir},i\downarrow} + E_{\text{dif},i\downarrow})\left(\frac{1 + \cos\alpha_i}{2} - \text{SVF}_i \right) \bigg/ \frac{1}{n}\sum_{i=1}^{i=n} \sec\alpha_i \quad (14)$$

Figures 3a–3f show the downward SSR flux explicitly calculated at the sub-grids with the resolution of 3″, which is the same as the DEM data, converted to the model grids with the horizontal resolutions ranging from 0.025° to 0.8° according to Equations 12–14. Compared to the downward SSR flux calculated over the plane surface (Figure 3g), it is clear that the sub-grid scale terrains strongly affect the intensity and spatial distribution of downward SSR flux at grid scale no matter of the grid resolutions. The regionally averaged annual mean downward SSR in Figures 3a–3f is about 8.4% less than that in Figure 3g. Therefore, a satisfactory description of the 3DSTSRE is essential for the numerical models, regardless of the model resolution.
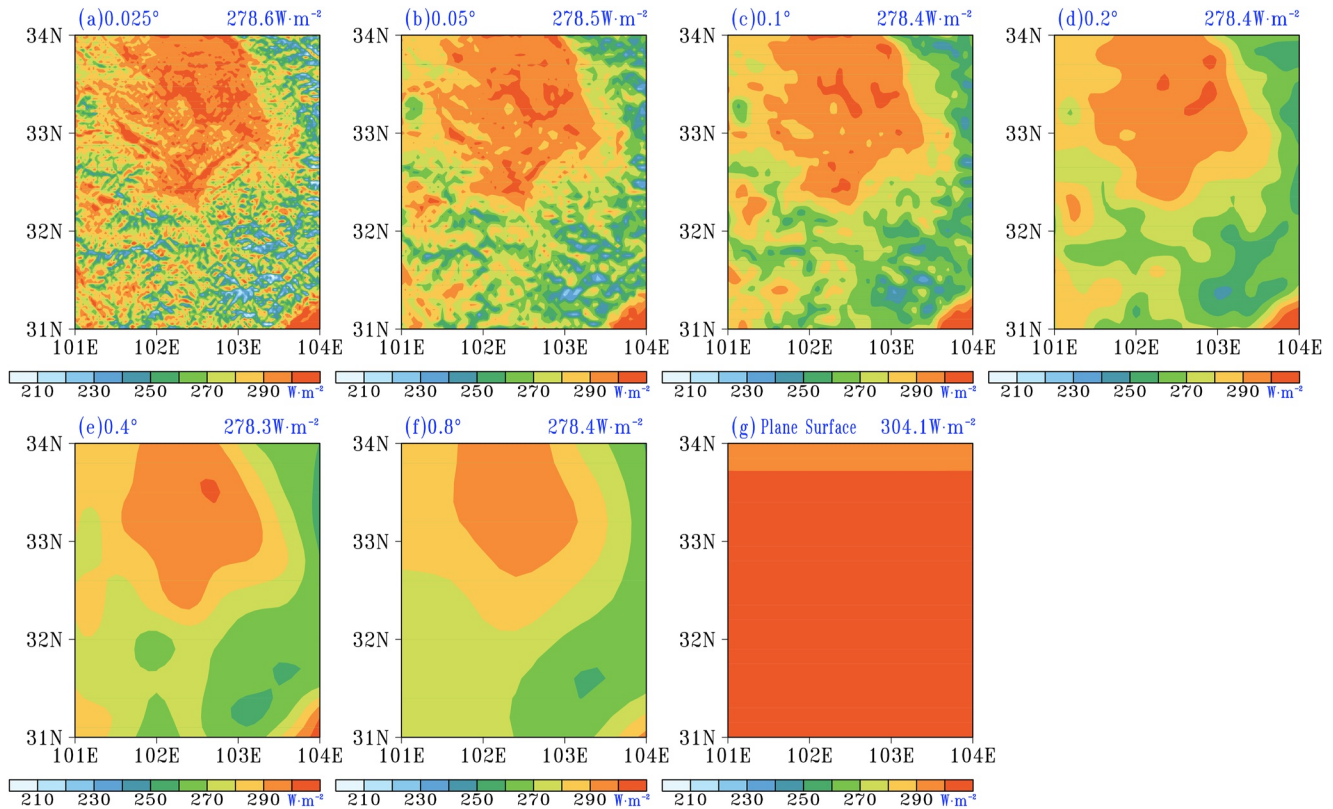
Figure 3. The annual mean downward surface solar radiation (SSR) flux explicitly calculated at the sub-grids with the horizontal resolution of 3″(∼90m) converted into the model grids with the horizontal resolution ranging from 0.025° to 0.8° according to Equations 12–14 (a–f) and the annual mean downward SSR flux over the plane surface (g) over Reg2 (Figure 2c). The number in the upper right corner of each pannel indicates the regionally averaged annual mean downward SSR flux.

2.2. Parameterization Scheme of 3DSTSRE

As shown in Figure 4, the clear-sky 3DSTSRE parameterization scheme is developed by 3 steps: (a) generate the global basic datasets of sub-grid terrain parameters including terrain slope, aspect, sky view factor, and maximal topographic elevation angle based on the SRTM4.1 data with a horizontal resolution of 3″ (∼90m); (b) prepare the grid-scale correction factors for a given model horizontal resolution in advance before the model integration; (c) develop a clear-sky 3DSTSRE scheme to correct the downward SSR components calculated by the radiation scheme of plane surface during the model integration.

Following Gu et al. (2020), we extract the 3DSTSRE correction factors derived from the global basic datasets of sub-grid terrain parameters before the model integration. Thus, the downward SSR components at model grids are calculated with considering the effect of 3D sub-grid terrain configuration during the model integration as follows:

$$E_{\text{dirt},p\downarrow} = \max\left(\text{SFC}_p \cdot \text{DIR}C_p \frac{E_{dir,p\downarrow}}{\cos Z_p}/\text{SEC}A_p, 0.0\right) \tag{15}$$

$$E_{\text{dift},p\downarrow} = \begin{cases} E_{\text{dif},p\downarrow}\left[\dfrac{E_{\text{dirt},p\downarrow}}{E_{ac}} + \text{DIF}C_p\left(1 - \dfrac{E_{\text{dir},p\downarrow}}{E_{ac}}\right)/\text{SEC}A_p\right], \; if \; \text{DIR}C_p > 0 \\[3mm] E_{\text{dif},p\downarrow}\left[\text{DIF}C_p\left(1 - \dfrac{E_{\text{dir},p\downarrow}}{E_{ac}}\right)/\text{SEC}A_p\right], \; \text{otherwise} \end{cases} \tag{16}$$

$$E_{\text{reft},p\downarrow} = (E_{\text{dir},p\downarrow} + E_{\text{dif},p\downarrow})\, a_p\text{REF}C_p/\text{SEC}A_p \tag{17}$$

$$\text{DIR}C_p = \cos Z_p + \text{TAC}B_p \sin Z_p \cos \theta_p + \text{TAS}B_p \sin Z_p \sin \theta_p \tag{18}$$
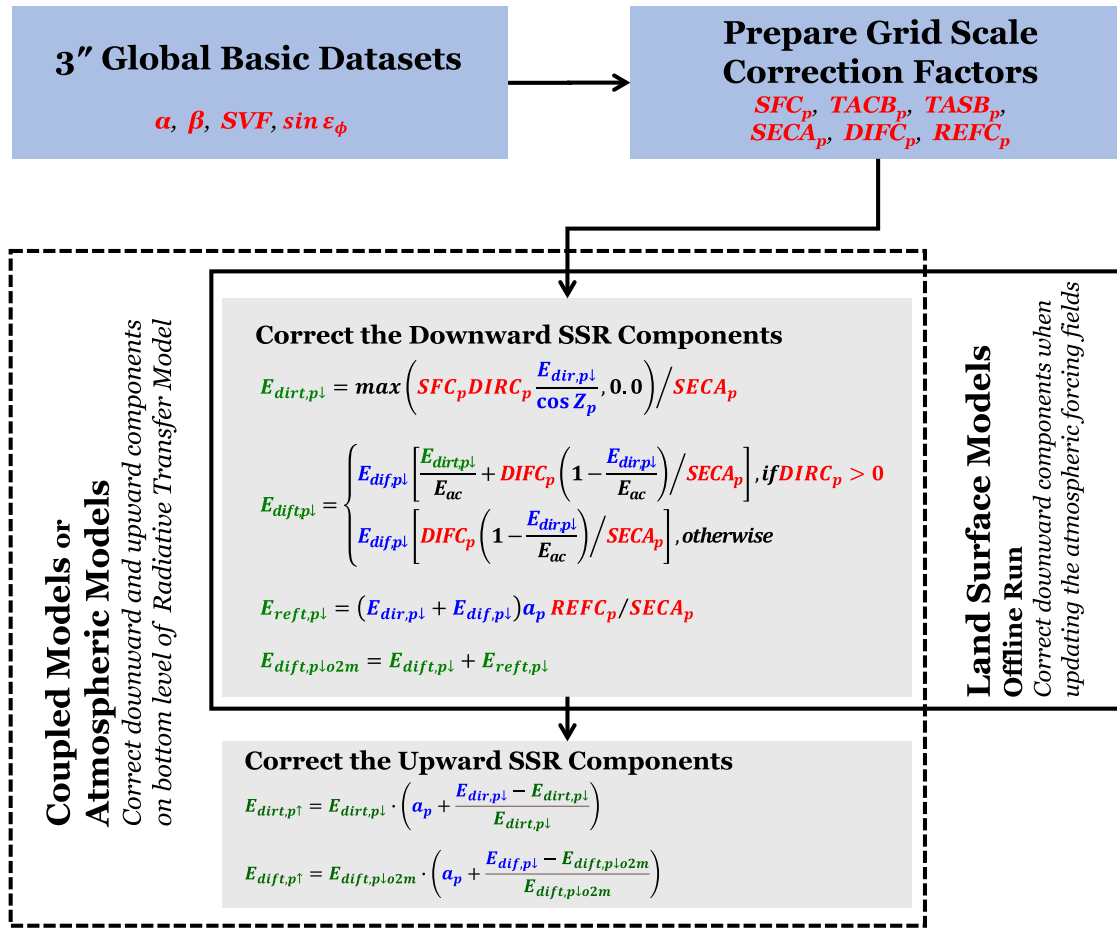
Figure 4. Diagrammatic sketch for the applications of the clear-sky 3-dimensional sub-grid terrain solar radiative effect (3DSTSRE) scheme in numerical models. The blue (gray) background indicates the process before (during) the model integration. The dashed (solid) box indicates the applications of the clear-sky 3DSTSRE scheme in numerical models. The red, blue, and green characters indicate the topographic elements, the original variables calculated in the numerical models, and the original variables corrected by the clear-sky 3DSTSRE scheme.

$$TACB_p = <\tan\alpha_i \cos\beta_i>_{i\to p} = \frac{1}{n}\sum_{i=1}^{i=n}\tan\alpha_i \cos\beta_i \tag{19}$$

$$TASB_p = <\tan\alpha_i \sin\beta_i>_{i\to p} = \frac{1}{n}\sum_{i=1}^{i=n}\tan\alpha_i \sin\beta_i \tag{20}$$

$$SECA_p = <\sec\alpha_i>_{i\to p} = \frac{1}{n}\sum_{i=1}^{i=n}\sec\alpha_i \tag{21}$$

$$DIFC_p = <\frac{\sec\alpha_i \cdot SVF_i}{2}(1+\cos\alpha_i)>_{i\to p} = \frac{1}{n}\sum_{i=1}^{i=n}\frac{\sec\alpha_i \cdot SVF_i}{2}(1+\cos\alpha_i) \tag{22}$$

$$REFC_p = <\left(\frac{1+\cos\alpha_i}{2}-SVF_i\right)\sec\alpha_i>_{i\to p} = \frac{1}{n}\sum_{i=1}^{i=n}\left(\frac{1+\cos\alpha_i}{2}-SVF_i\right)\sec\alpha_i \tag{23}$$

$$SFC_p = <SF_i>_{i\to p} \tag{24}$$

The operator $<>_{i\to p}$ stands for the process of aggregating the variables at the sub-grid scale to the grid scale. We ignore the differences in the surface albedo a, solar zenith angle Z, solar azimuth angle θ, atmospheric transmittance τ_b of direct solar radiation, and transmittance τ_d of diffuse solar radiation among the sub-grids

within a model grid. The grid-scale time-invariable correct factors $\mathrm{TAC}B_p$, $\mathrm{TAS}B_p$, $\mathrm{SEC}A_p$, $\mathrm{DIF}C_p$, and $\mathrm{REF}C_p$ related to the 3D configuration of sub-grid terrain are simply derived from the arithmetic mean of all sub-grids within a given model grid before the model integration.

It is difficult to obtain the grid-scale SFC_p by a formula because it is a time-variant variable jointly determined by the solar azimuth angle and zenith angle at every model time step. As mentioned in Zhang et al. (2022), we generate the grid-scale SFC_p by a statistical method as follows: First, we divide $\sin\varepsilon_{\phi_k}$ which ranges from 0 to 1 into $M = 100$ levels ($\sin\varepsilon_{\phi_k} \leq 0.01$, $\sin\varepsilon_{\phi_k} \leq 0.02$, ..., and $\sin\varepsilon_{\phi_k} \leq 1$) on sub-grids at 360 azimuth directions. Second, we count the total number of sub-grids with $\sin\varepsilon_{\phi_k} \leq 0.01$, $\sin\varepsilon_{\phi_k} \leq 0.02$, ..., $\sin\varepsilon_{\phi_k} \leq 1$ at a given azimuth direction within a model grid with a given horizontal resolution, that is, there are n_1, n_2, ..., n_{100} sub-grids with $\sin\varepsilon_{\phi_k} \leq 0.01$, $\sin\varepsilon_{\phi_k} \leq 0.02$,..., $\sin\varepsilon_{\phi_k} \leq 1$ in the model grid $p(IX, JY)$ (IX and JY represent the number of the model grid in the longitudinal and latitudinal directions, respectively) with n sub-grids at a given azimuth direction, respectively, then we can get the ratio of total sub-grids with $\sin\varepsilon_{\phi_k} \leq 0.01$, $\sin\varepsilon_{\phi_k} \leq 0.02$, $\sin\varepsilon_{\phi_k} \leq 0.02$,..., $\sin\varepsilon_{\phi_k} \leq 1$ to the total sub-grids within the model grid $p(IX, JY)$ by n_1/n, n_2/n, …, n_{100}/n at each azimuth direction, respectively. Adopting the same method, we can get the ratios of total sub-grids with different levels of $\sin\varepsilon_{\phi_k}$ to the total sub-grids within each model grid at the 360 azimuth directions. Finally, we use a time-invariant four-dimensional array $A(I\mathrm{num}, J\mathrm{num}, M, N)$ to save these ratios, Inum and Jnum denote the numbers of model grids in the longitudinal and latitudinal directions, respectively. M and N are the total levels of $\sin\varepsilon_{\phi_k}$ and the total azimuth directions divided. Generally, larger M and N can get more accurate SFC_p. In current study we divide the $\sin\varepsilon_{\phi_k}$ at 360 azimuth directions ($N = 360$) into 100 levels ($M = 100$) with the consideration of the balance between the precision and the minimization of computational demand. As mentioned above, the time-invariant four-dimensional matrix $A(\mathrm{Inum}, \mathrm{Jnum}, M, N)$ only determined by the maximal topographic elevation angle ε_{ϕ_k} at sub-grid scale is prepared in advance before the model integration.

To calculate the downward SSR components with considering the effects of the 3D configuration of sub-grid terrains, the clear-sky 3DSTSRE parameterization scheme is developed based on Equations 15–24, which involve the grid-scale time-invariable factors ($\mathrm{TAC}B_p$, $\mathrm{TAS}B_p$, $\mathrm{SEC}A_p$, $\mathrm{DIF}C_p$, and $\mathrm{REF}C_p$) and time-variable factor SFC_p determined by the time-invariant four-dimensional matrix $A(I\mathrm{num}, J\mathrm{num}, M, N)$ and grid-scale time-variable Z_p and θ_p. The $\mathrm{TAC}B_p$, $\mathrm{TAS}B_p$, $\mathrm{SEC}A_p$, $\mathrm{DIF}C_p$, $\mathrm{REF}C_p$, and $A(I\mathrm{num}, J\mathrm{num}, M, N)$ calculated in advance are input at the first time step of the model integration. Meanwhile, the grid-scale variables a_p, Z_p, θ_p, $E_{\mathrm{dir},p}$, and $E_{\mathrm{dif},p}$ in each model grid are calculated based on the radiation scheme of plane surface at every time step during the model integration. The SFC_p at the model grid $p(IX, JY)$ can be derived from the nearest order of IK and IL for the grid-scale solar azimuth angle θ_p and zenith angle Z_p. The SFC_p ranging from 0 to 1 (zero for completely shadowed) indicates that the fraction of the sub-grids with the $\sin\varepsilon_{\theta_p} \leq \cos Z_p$ is not shadowed in a given model grid at a given time, that is, for the model grid $p(IX, JY)$ with the grid-scale $\cos Z_p = 0.25$ and solar azimuth angle $\theta_p = 100°$, $IK = 0.25/(1/M)$ and $IL = \mathrm{int}[(100° - 0°)/(360°/N)] + 1$. In current study, $M = 100$ and

$N = 360$, so $IK = 25$ and $IL = 101$. Note that $IL = \begin{cases} 101 \text{ if } (100° \leq \theta_p \leq 100.5°) \\ 102 \text{ if } (100.5° < \theta_p \leq 101°) \end{cases}$. SFC_p at the model grid

$p(IX, JY)$ with $\cos Z_p = 0.25$ and $\theta_p = 100°$ can be easily taken from the value of $A(IX, JY, 25, 101)$.

The grid-scale downward SSR components with the consideration of 3DSTSRE are calculated every time step in terms of the methods indicated above. However, the parameterized calculations of downward SSR components based on Equations 15–24 show large negative biases compared to those derived from the explicit calculations of Equations 12–14 (not shown). The negative biases are mainly attributed to the parameterized calculation of downward direct solar radiation (Equation 15), specifically the simplified replacement of $< \sec\alpha_i \cdot \cos I_i \cdot SF_i >_{i \to p}$ with $< \sec\alpha_i \cdot \cos I_i >_{i \to p} < SF_i >_{i \to p}$ without considering the regional mean product of their perturbation terms, resulting in the overestimation of terrain shadow effect. These negative biases are the main error source of the preliminary version of clear-sky 3DSTSRE scheme (Zhang et al., 2022). To reduce the error in the preliminary clear-sky 3DSTSRE scheme, the SFC_p related to the shadow effect of surrounding terrains in Equation 24 is further adjusted by:

$$\mathrm{SFC}_p = 1 - C_{\mathrm{ad}} (1 - < \mathrm{SF}_i >_{i \to p}) \tag{25}$$

$$C_{\mathrm{ad}} = 0.1849 dx^{-1.443} + 0.04561 \tag{26}$$

C_{ad} is an adjustment factor depending on the model horizontal resolution dx (Figure 8), it ranges from 0 to 1. $C_{\mathrm{ad}} = 1$ (0) indicates that the shadow effect of surround terrains is (is not) considered. C_{ad} greatly reduces the error of the preliminary version of clear-sky 3DSTSRE scheme (Zhang et al., 2022). The error source of the parameterized calculation of downward direct solar radiation (Equation 15) and the specific reason for the adoption of Equations 25 and 26 are discussed in Section 3.

There are no variables representing the reflected solar radiation from the surrounding terrain ($E_{\mathrm{reft},p\downarrow}$ in Equation 17) in the numerical models. $E_{\mathrm{reft},p\downarrow}$ is added to $E_{\mathrm{dift},p\downarrow}$ following previous studies (Arnold et al., 2006; Helbig et al., 2009, 2010; Hock & Holmgren, 2005; Senkova et al., 2007):

$$E_{\mathrm{dift},p\downarrow o2m} = E_{\mathrm{dift},p\downarrow} + E_{\mathrm{reft},p\downarrow} \tag{27}$$

where $E_{\mathrm{dift},p\downarrow}$ ($E_{\mathrm{reft},p\downarrow}$) is calculated by Equations 16 and 17 and $E_{\mathrm{dift},p\downarrow o2m}$ is the downward diffuse solar radiation calculated by the 3DSTSRE scheme in the numerical models.

In land surface models (LSMs), the downward SSR components play a role as variables of the atmospheric forcing field. In the offline run of LSMs, the downward SSR components are corrected according to Equations 15–17 when updating the atmospheric forcing fields. However, the upward SSR components should be also corrected to ensure the energy conservation (Lee et al., 2015) when applying the 3DSTSRE scheme to coupled or atmospheric models, in which the 3DSTSRE scheme is applied to the bottom level of the radiative transfer module. The upward SSR components on the bottom level of atmosphere should be adjusted by:

$$E_{\mathrm{dirt},p\uparrow} = E_{\mathrm{dirt},p\downarrow} \cdot \left(a_p + \frac{E_{\mathrm{dir},p\downarrow} - E_{\mathrm{dirt},p\downarrow}}{E_{\mathrm{dirt},p\downarrow}} \right) \tag{28}$$

$$E_{\mathrm{dift},p\uparrow} = E_{\mathrm{dift},p\downarrow o2m} \cdot \left(a_p + \frac{E_{\mathrm{dif},p\downarrow} - E_{\mathrm{dift},p\downarrow o2m}}{E_{\mathrm{dift},p\downarrow o2m}} \right) \tag{29}$$

where $E_{\mathrm{dirt},p\uparrow}$ ($E_{\mathrm{dift},p\uparrow}$) is the upward direct (diffuse) solar radiation flux calculated by the 3DSTSRE scheme.

2.3. Data

The Shuttle Radar Topography Mission (SRTM) 90m Digital Elevation Database v4.1 (Jarvis et al., 2008) are used to generate the terrain slope, aspect, sky view factor and shadow factor in this study. The SRTM V4.1 is a further processed and hole-filled version of the original NASA SRTM data (Reuter et al., 2007). The biases of the SRTM data in mountainous areas are larger than those in flat areas (Gorokhovich & Voustianiouk, 2006; Rodriguez et al., 2006). However, the SRTM data still provide a precious opportunity for a detailed terrain description. Thus, the SRTM V4.1 data are widely applied in geophysical studies over mountains (Frey & Paul, 2012; Lee et al., 2013; Sreedevi et al., 2013).

Following Li and Luo (2015), the MODIS MCD43A3 with a resolution of 500 m (shortwave band) offers the albedo in this study (Schaaf & Wang, 2015). The MODIS albedo data are interpolated onto the SRTM grid with a resolution of 3″ by bilinear interpolation method. The albedo data on the model grids with the resolutions of 0.025°, 0.05°, 0.1°, 0.2°, 0.4°, and 0.8° are the arithmetic average of MODIS data within each model grid.

This study tests the clear-sky 3DSTSRE parameterization scheme in 3 sub-regions (Figures 2b–2d) with rugged terrains (Reg1, 35°E ∼ 40°E, 5°N ∼ 10°N; Reg2, 100°E ∼ 105°E, 30°N ∼ 35°N; Reg3, 130°E ∼ 135°E, 55°N ∼ 60°N). According to the sky view factor in Figure 2, Reg2 situated in the eastern Tibetan Plateau has the most complex terrain among the 3 sub-regions. Reg1 in the Great Rift Valley (Reg3 including parts of the Wai Hinggan Mountains) is featured by rugged terrains near the equator (Arctic Circle). Reg2 is the testing area for constructing the parameterization scheme because of its location of mid-latitude with rich terrain feature.

Table 1
Experimental Design

Group	Experiment name	Calculations	Grid resolution
G1	EXPL-cosISF	Explicit calculation of the downward direct solar radiation with the effect of terrain self and cast shadows in the mountain radiation theory: $\max\left(SF \cdot \tau_b \cdot E_{ac}\left(\frac{r_0}{r}\right)^2 \cos I, 0.0\right)$	3″ (~90m)
	EXPL-cosI	Explicit calculation of the downward direct solar radiation with the effect of terrain self shadow in the mountain radiation theory: $\max\left(\tau_b \cdot E_{ac}\left(\frac{r_0}{r}\right)^2 \cos I, 0.0\right)$	
	EXPL-SF	Explicit calculation of the downward direct solar radiation with the effect of terrain cast shadow in the mountain radiation theory: $\max\left(SF \cdot \tau_b \cdot E_{ac}\left(\frac{r_0}{r}\right)^2 \cos Z, 0.0\right)$	
	EXPL-Plane	Explicit calculation of the downward direct solar radiation based on the plane radiation theory $\max\left(\tau_b \cdot E_{ac}\left(\frac{r_0}{r}\right)^2 \cos Z, 0.0\right)$	
	PARA-cosISF	Parameterized calculation of the downward direct solar radiation on model grids with the effect of sub-grid terrain self and cast shadows: $\max\left(SFC_p DIRC_p \frac{E_{dir,p\downarrow}}{\cos Z_p}, 0.0\right)/SECA_p$	0.1°
	PARA-cosI	Parameterized calculation of the downward direct solar radiation on model grids with the effect of sub-grid terrain self shadow: $\max\left(DIRC_p \frac{E_{dir,p\downarrow}}{\cos Z_p}, 0.0\right)/SECA_p$	
	PARA-SF	Parameterized calculation of the downward direct solar radiation on model grids with the effect of sub-grid terrain cast shadow: $\max\left(SFC_p < \cos Z_i \sec\alpha_i >_{i\to p} \frac{E_{dir,p\downarrow}}{\cos Z_p}, 0.0\right)/SECA_p$	
	PARA-Plane	Parameterized calculation of the downward direct solar radiation on model grids based on the radiation scheme of plane surface: $\cos Z_p \tau_{b,p} E_{ac}\left(\frac{r_0}{r}\right)^2$	
G2	EXPL-TEST	Explicit calculation of downward SSR components at the grids of DEM data based on Equations 3–5	3″ (~90m)
	PARA-TEST	Parameterized calculation of the downward SSR components based on 15–23 and 25 at the model grids with different horizontal resolutions	0.025°, 0.05°, 0.1°, 0.2°, 0.4°, and 0.8°
G3	EXPL	Explicit calculation of downward SSR components at the grids of DEM data based on Equations 3–5	3″ (~90m)
	PARA-C_{ad}	Parameterized calculation of the downward SSR components based on Equations 15–23, 25	0.025°, 0.05°, 0.1°, 0.2°, 0.4°, and 0.8°
	PARA-NoC_{ad}	Parameterized calculation of the downward SSR components based on Equations 15–24	

2.4. Experimental Design

As shown in Table 1, we set up three groups of experiments with the aim to analyze the error source of the parameterized calculation of direct solar radiation flux based on the results of experiment group G1, test the optimal value of the adjustment parameter C_{ad} with the results of experiment group G2, and evaluate the performance of the clear-sky 3DSTSRE parameterization scheme by conducting the experiment group G3. The experiments with prefix EXPL explicitly calculate the downward SSR components in the sub-grids of 3″, which are then area-weighted averaged to the grids with different resolutions (i.e., 0.025°, 0.05°, 0.1°, 0.2°, 0.4°, and 0.8°). The experiments with prefix PARA calculate the downward SSR components with different resolutions by the clear-sky 3DSTSRE parameterization scheme.

To reveal the error source of the parameterized calculation of direct solar radiation flux, we carry out 8 sensitive experiments in the experiment group G1 over Reg2 (Table 1). The $\cos Z$, $\cos I$, and SF with a resolution of 3″ calculated in the EXPL-cosISF experiment are used to statistically produce the correction factors $DIRC_p$, SFC_p, and $<\cos Z_i \cdot \sec\alpha_i>_{i\to p}$ for the PARA-cosISF, PARA-cosI, and PARA-SF experiments. The $DIRC_p$ and SFC_p (Equations 18 and 24) in the clear-sky 3DSTSRE parameterized scheme are evaluated by the $DIRC_p$ and SFC_p derived from the explicit calculations of the EXPL-cosISF experiment.

To achieve the optimal value of the adjustment parameter C_{ad} to correct the SFC_p, in the experiment group G2 (Table 1), we carried out a series of parameterized experiments with different C_{ad} to estimate the downward SSR flux in Reg2 at a given horizontal resolution, for which the optimal C_{ad} is obtained when the root mean square error of the instant downward SSR at all the time steps throughout the year calculated in the PARA-TEST against those derived from the explicit calculations of EXPL-TEST is the smallest. Then we can obtain the

optimal C_{ad} at each horizontal resolutions (Table 1) and further get the fitting relation between the optimal C_{ad} and model horizontal resolution (Equation 25). For a given resolution grid, C_{ad} is tested between 1.0 and 0.0 based on the half-interval search algorithm (Williams, 1976). Specifically, we first calculated the downward SSR flux by the clear-sky 3DSTSRE parameterization scheme with $C_{ad} = (1.0 + 0.0)/2 = 0.5$. If the clear-sky 3DSTSRE parameterization scheme with $C_{ad} = 0.5$ produces large root mean square error in the downward SSR, then we calculate the downward SSR flux by the clear-sky 3DSTSRE scheme with $C_{ad} = (0.5 + 0.0)/2 = 0.25$ ($C_{ad} = (0.5 + 1.0)/2 = 0.75$)……, until we get the optimal C_{ad} value.

We further carried out the experiment group G3 to indicate the impact of SFC_p adjusted by the optimal C_{ad} (Equations 25 and 26) on the accuracy of the clear-sky 3DSTSRE scheme with different horizontal resolutions over Reg1, Reg2, and Reg3. The experiment PARA-C_{ad} (PARA-NoC_{ad}) adopts the clear-sky 3DSTSRE scheme with (without) the adjustment of SFC_p.

All experiments calculate the downward SSR flux on the 15th day of each month in 2010 under clear sky conditions with the time step of 20 min. Each run starts from 00:00 UTC and ends at 24:00 UTC on the 15th day of each month in 2010. The mean value of the results on the 15th day of each month is taken as the annual mean.

2.5. Evaluation Metrics

The metrics such as the spatial correlation coefficient (SCC), root mean square error, normalized mean absolute error (NMAE), relative error (RE), and Taylor score (TS) (Taylor, 2001) are adopted to evaluate the clear-sky 3DSTSRE parameterization scheme. The lower (higher) error, NMAE, and RE (SCC and TS) indicate better performance. To compare the scheme performance in different regions and at different time, the mean absolute error is normalized by the mean value of the year, the day, or the region. Many previous studies have proven the reliability of the mountain radiation theory by validation with observations (Aguilar et al., 2010; Dubayah & Loechel, 1997; Fu & Rich, 1999; Oliphant et al., 2003; Ruiz-Arias et al., 2011; Tovar-Pescador et al., 2006; Yan et al., 2021). Therefore, the downward SSR components produced by the EXPL-cosISF, EXPL-TEST, and EXPL experiments are treated as the true values in this study.

3. Error Source of the Clear-Sky 3DSTSRE Parameterization Scheme and Solution to Reduce Error

3.1. Error Source of the Clear-Sky 3DSTSRE Parameterization Scheme

As shown in Figure 1d, the direct solar radiation flux is affected by the terrain self shadow and surrounding terrain cast shadow (Corripio, 2003; Olson & Rupper, 2019). $\cos I$ (SF) is a measure of the terrain self shadow (cast shadow) effects. According to $\cos I = \cos Z \cdot \cos \alpha + \sin \alpha \cdot \sin Z \cdot \cos(\beta - \theta)$, the slope receives more direct solar radiation when the difference between the solar azimuth and the terrain aspect is less than 90° (green part in Figure 1d). The slope receives less direct solar radiation flux which is terrain self shadowed when the angle between the solar azimuth and the terrain aspect is larger than 90° (pink part in Figure 1d). The shadow of the surrounding terrain also reduces local direct solar radiation (violet part in Figure 1d). In the continuous mountains, the terrain self shadow and cast shadow often occur together in the same place at the same time (gray part in Figure 1d).

The differences in direct solar radiation flux at surface between the EXPL-Plane and PARA-Plane experiments with the horizontal resolution of 0.1° are quite small (0.1 W·m^{-2}, not shown). Therefore, the differences in latitude, solar zenith, and solar azimuth between the grid and sub-grid are indeed ignorable. The differences in direct solar radiation flux at surface between the EXPL-cosISF and EXPL-Plane experiments with the resolution of 3″ (~90m) represent the total terrain effects on the direct solar radiation (Figure 5a). The total terrain effects mainly reduce the surface direct solar radiation flux by the terrain self and cast shadow. The differences of direct solar radiation flux at surface between the EXPL-cosI (EXPL-SF) and EXPL-Plane experiments represent the impact of terrain self (cast) shadow (Figures 5b and 5c). It is clear that both the terrain self and cast shadow largely affect the direct solar radiation flux over the regions featured by valleys with the sky view factor less than 0.8 (Figure 2c), where the annual mean direct solar radiation flux can be reduced by more than 30 (20) W·m^{-2} due to the effect of terrain self (cast) shadow.
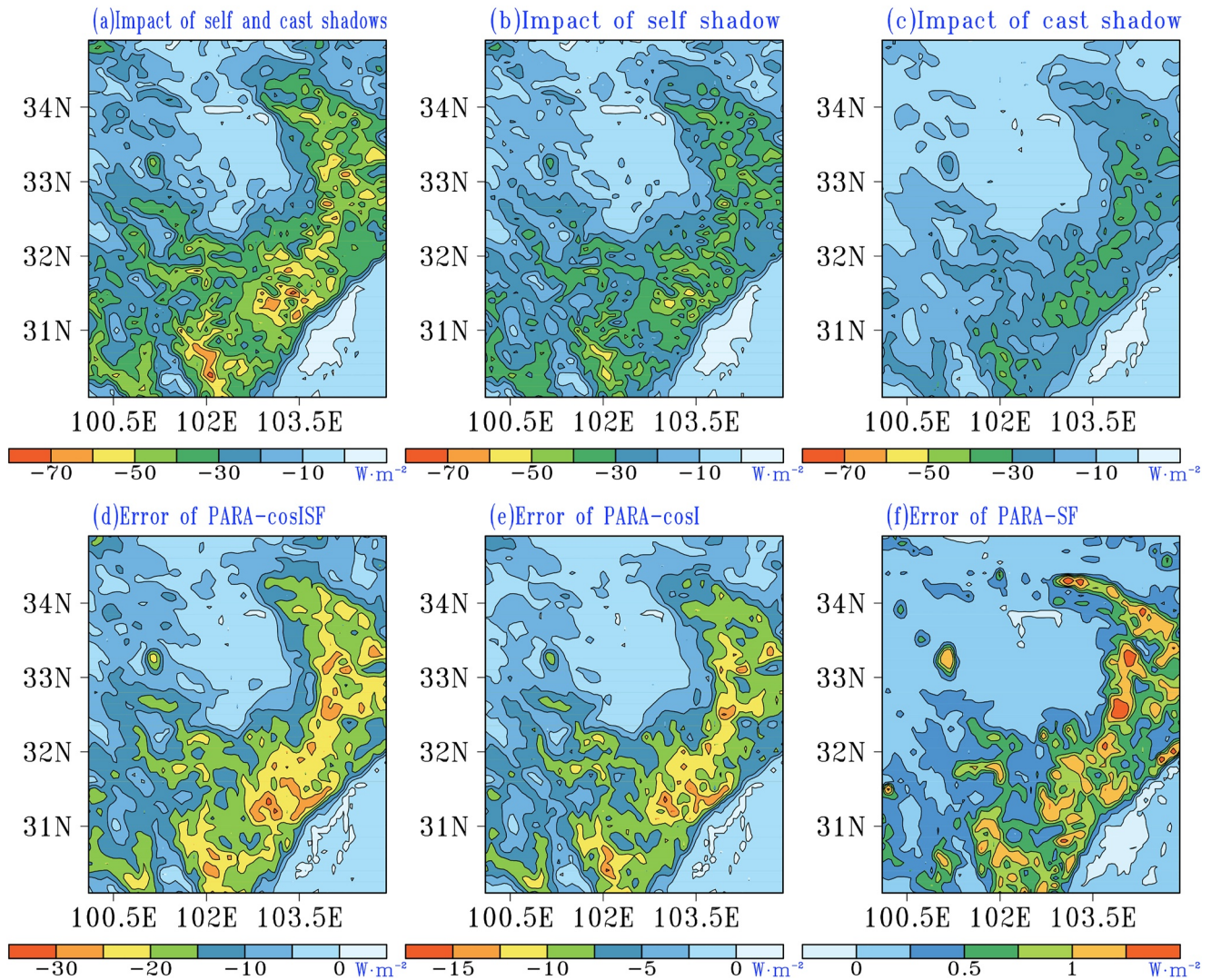
Figure 5. Impacts of terrain (a) self and cast shadows, (b) self shadow, and (c) cast shadow on the annual mean downward direct solar radiation flux at surface with the grid resolution of 0.1°, which are derived from the differences between EXPL-cosISF and EXPL-Plane, between EXPL-cosI and EXPL-Plane, between EXPL-SF and EXPL-Plane at the grid resolution of 3″, respectively. The errors in the annual mean downward direct solar radiation at surface produced by the (d) PARA-cosISF, (e) PARA-cosI, and (f) PARA_SF experiments with the grid resolution of 0.1° against those derived from the explicit calculations of EXPL-cosISF experiment with the resolution of 3″ over the Reg2 (Figure 2c).

The differences in direct solar radiation flux at surface between the PARA-cosISF calculations with the horizontal resolution of 0.1° and those derived from the explicit calculations of EXPL-cosISF indicate the total errors of clear-sky 3DSTSRE parameterization scheme (Figure 5d). And the differences between the PARA-cosI (PARA-SF) and EXPL-cosI (EXPL-SF) experiments represent the errors resulted from the parameterization of terrain self (cast) shadow effect (Figures 5e and 5f). As shown in Figure 5d, it can be noted that the clear-sky 3DSTSRE scheme tends to underestimate the direct solar radiation flux, especially over the complex terrains featured by the sky view factor less than 0.8 (Figure 2c), where the direct solar radiation flux is underestimated by more than 20 W·m^{-2} due to the overestimation of parameterized terrain shadow effect. Comparison of Figures 5d and 5e suggests that the errors resulted from the parameterized terrain self shadow effect mainly contribute to the total errors of the clear-sky 3DSTSRE scheme. The overestimation of the parameterized terrain self shadow comes from the process of DIRC$_p$ = < secα_i · cosI_i >$_{i \to p}$ in Equation 18. The value of cos I ranges from −1 to 1. The value of sec α is non-negative. So the secα_i · cosI_i at the sub-grids in the gray and pink parts in Figure 1d is negative. The negative secα_i · cosI_i turns to 0 at sub-grids in the EXPL-cosISF and EXPL-cosI experiments, which means there is no direct solar radiation flux. However, when calculating the grid scale DIRC$_p$ by
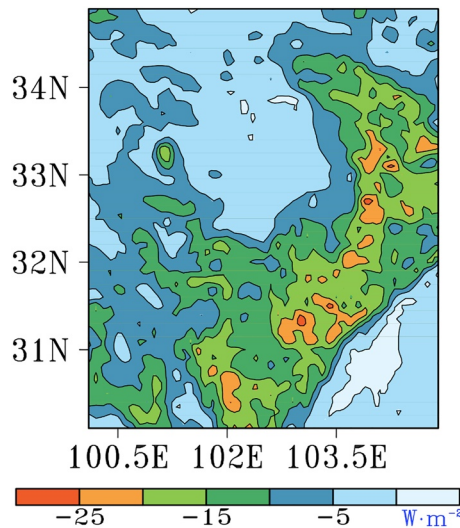
Figure 6. The overlapping impact (gray area in Figure 1d) of the terrain self and cast shadows on the annual mean downward direct solar radiation flux at surface over Reg2 (Figure 2c) at resolution of 0.1°, which is derived from the difference between the sum of values in Figures 5b and 5c and those in Figure 5a.

Equation 18, the negative $\sec\alpha_i \cdot \cos I_i$ cannot be turned to 0, and the negative values of $\sec\alpha_i \cdot \cos I_i$ are averaged into DIRC_p, and therefore the overestimated terrain self shadow effect in the clear-sky 3DSTSRE scheme leads to the underestimation of downward direct solar radiation flux at surface.

Meanwhile, the total errors resulted from the separately parameterized terrain self and cast shadow effects (Figures 5e and 5f) cannot explain the errors produced by the clear-sky 3DSTSRE scheme. Another main source of the errors is the overestimation of the overlapping impact of the terrain self and cast shadow effects (Figure 6) in the process of $< \sec\alpha_i \cdot \cos I_i >_{i\to p} < \mathrm{SF}_i >_{i\to p}$. In the process of $< \sec\alpha_i \cdot \cos I_i \cdot \mathrm{SF}_i >_{i\to p}$ (explicit calculation), the direct solar radiation at the sub-grids in the gray part of Figure 1d is 0. The terrain cast shadow together with self shadow affects the grid scale direct solar radiation flux at surface once. However, during the process of $< \sec\alpha_i \cdot \cos I_i >_{i\to p} < \mathrm{SF}_i >_{i\to p}$ (parameterized calculation), the terrain cast shadow and self shadow in the gray parts at the sub-grids in Figure 1d repeatedly affect the grid scale direct solar radiation flux at surface. The sum of terrain self shadow effect (Figure 5b) and the surrounding terrain cast shadow effect (Figure 5c) subtracted by the total terrain effects (Figure 5a) indicates the overlapping part (gray area in Figure 1d) of the terrain self and cast shadow effects (Figure 6), which largely contributes to the errors of clear-sky 3DSTSRE scheme (Figure 5d).

In the clear-sky 3DSTSRE scheme, the synergistic effect of terrain self and cast shadows is indicated by $\mathrm{DIRC}_p \cdot \mathrm{SFC}_p$ (Equation 15). Figure 7 shows the relative errors of parameterized DIRC_p and SFC_p with the horizontal resolution of 0.1° relative to those derived from the explicit calculations of the EXPL-cosISF experiment with the resolution of 3″. The relative error of parameterized DIRC_p is within $\pm 0.3\%$ (Figure 7a), while the parameterized SFC_p is overestimated by up to 2% of relative errors (Figure 7b), which are relatively larger compared to the DIRC_p. The overestimation of SFC_p weakens the surrounding terrain cast shadow effect. Overall, the parameterized DIRC_p and SFC_p are basically mathematically accurate despite of the errors produced by the clear-sky 3DSTSRE scheme due to the physical processing, that is, the negative values of direct solar radiation flux at some sub-grids are taken into the parameterization. Therefore, we further adjust the SFC_p by the adjustment factor C_{ad} (Equations 25 and 26) to reduce the errors of clear-sky 3DSTSRE scheme resulted from the overlapping effect of terrain self and cast shadow (Figure 6).

3.2. Solution to Reduce Error

It is difficult to determine the exact ratio of the sub-grids with $\sec\alpha_i \cdot \cos I_i < 0$ or the sub-grids with $\sec\alpha_i \cdot \cos I_i < 0$ and $\mathrm{SF}_i = 0$. However, we can make a compromise to meet the goal. Specifically, we replace $< \sec\alpha_i \cdot \cos I_i \cdot \mathrm{SF}_i >_{i\to p}$ with $(1 - C_{\mathrm{ad}}(1 - < \mathrm{SF}_i >_{i\to p})) \cdot < \sec\alpha_i \cdot \cos I_i >_{i\to p}$ (Equations 15 and 25). $< \sec\alpha_i \cdot \cos I_i >_{i\to p}$ stands for the grid-scale self terrain effect and the area weight. $(1 - C_{\mathrm{ad}}(1 - < \mathrm{SF}_i >_{i\to p}))$ stands for the adjusted grid-scale shadow factor. $1 - < \mathrm{SF}_i >_{i\to p}$ is the ratio of all the cast shadowed sub-grids. $C_{\mathrm{ad}}(1 - < \mathrm{SF}_i >_{i\to p})$ is the ratio of the cast shadowed sub-grids with $\sec\alpha_i \cdot \cos I_i > 0$.

The value of C_{ad} is tested in Reg2 with the horizontal resolutions of 0.025°, 0.05°, 0.1°, 0.2°, 0.4°, and 0.8°. The adjust factor C_{ad} is optimal when the root mean square error of the parameterized downward SSR is the smallest. The optimal C_{ad} values are 0.1, 0.064, 0.054, 0.05, 0.048, and 0.043 for the 0.025°, 0.05°, 0.1°, 0.2°, 0.4°, and 0.8° model grids, respectively. The grid resolutions (°) converted to distances (km) are 2.3446, 4.6893, 9.3785, 18.7570, 37.5141, and 75.0281 km ($dx = 111.2\mathrm{km} \times \mathrm{res} \times \cos(32.5°)$). *res* is the resolution in degrees. 32.5°N is the center latitude of Reg2. We get
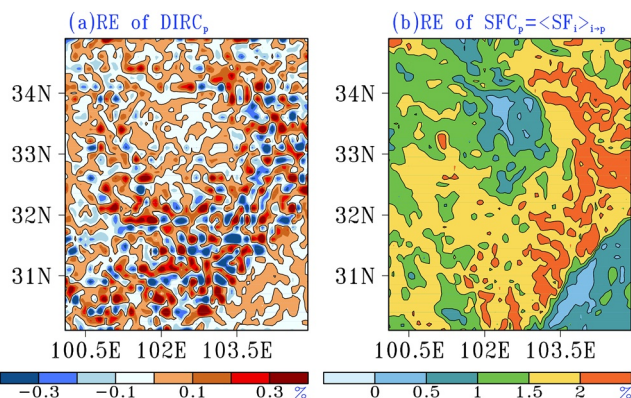

Figure 7. The relative errors of the parameterized (a) DIRC_p and (b) SFC_p over Reg2 (Figure 2c) with the grid resolution of 0.1°.
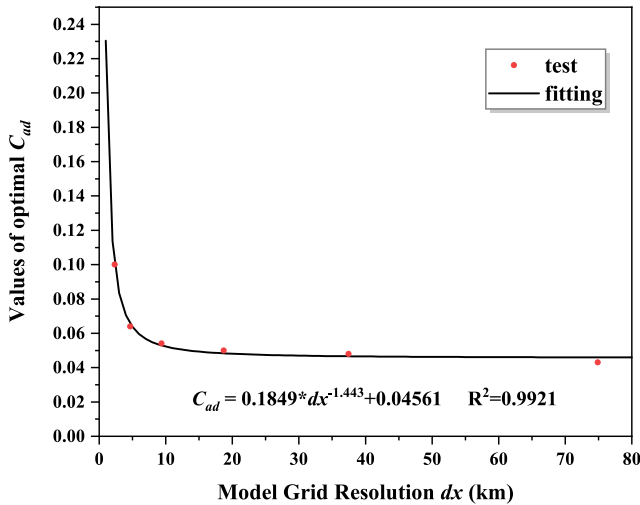
Figure 8. The values of optimal C_{ad} (red dots) at different resolutions and the fitting curve (black line) of the optimal C_{ad} with the grid resolutions based on the results over Reg2 (Figure 2c).

the function $C_{ad} = 0.1849dx^{-1.443} + 0.04561$ (Equation 26) through the least squares fitting, where dx is the model horizontal resolution in kilometers and is calculated by $dx = 111.2\text{km} \times \text{res} \times \cos\varphi$. As shown in Figure 8, the fitting curve of C_{ad} is in good agreement with the test values. The sum of squared errors (SSE) and the determination coefficient (R^2) are 1.72×10^{-5} and 0.99 in the fitting, suggesting that the function fits well. The portability of C_{ad} to the regions with different latitudes and terrains is tested over Reg1 and Reg3 and the results are shown in Section 4.

4. Scheme Evaluation

To evaluate the clear-sky 3DSTSRE parameterization scheme, we carried out the PARA-C_{ad} (PARA-NoC_{ad}) experiment with (without) the parameterized shadow factor SFC$_p$ adjusted by the factor C_{ad} (Equations 25 and 26) with the horizontal resolutions of 0.025°, 0.05°, 0.1°, 0.2°, 0.4°, and 0.8° in Reg1, Reg2, and Reg3, respectively. Figure 9 shows the normalized mean absolute error (NMAE) of the instant downward SSR flux throughout the year with the horizontal resolution of 0.1° relative to those derived from the explicit calculations of the EXPL experiment with the horizontal resolution of 3″. The PARA-C_{ad} experiment can well reproduce the spatial distribution of the annual mean downward SSR flux derived from the explicit calculations of EXPL experiment (Figures 9a, 9b, 9e, 9f, 9i and 9j). The NMAE of the downward SSR flux calculated by the PARA-C_{ad} experiment are less than 1% (Figures 9c, 9g and 9k). The NMAE of the downward SSR flux calculated by the PARA-NoC_{ad} experiment are more than 5% in the areas with very complex terrains (Figures 9d and 9h).

Although the relation between C_{ad} and dx (Equation 26) is fitted according to the experimental results over Reg2, the NMAEs in Figures 9c, 9d, 9k and 9l show that Equation 26 is successfully portable to Reg1 and Reg3. The high portability of Equation 26 over Reg1 and Reg3 indicates that Equation 26 can be extended to the other places of the world because of the quite different terrains and latitudes between Reg1, Reg3, and Reg2. The NMAE in the downward SSR flux calculated by the clear-sky 3DSTSRE scheme with other horizontal resolutions show very similar features to those with the 0.1° horizontal resolution (not shown), indicating the adjustment of SFC$_p$ can further remarkably reduce the relative errors of the annual mean downward SSR flux calculated by the clear-sky 3DSTSRE without the SFC$_p$ adjusted over the areas featured by complex terrains.

Figure 10 shows the probability distributions of the relative error for the instant downward SSR flux throughout the year calculated by the PARA-C_{ad} and PARA-noC_{ad} experiments over the 3 regions with different horizontal resolutions. The curves in Figure 10a are approximately the normal distribution while the curves in Figure 10b are the skewed distribution. The scheme without the adjustment factor C_{ad} generally underestimates the downward SSR fluxes due to the overestimation of the terrain shadow effect. Figure 10a shows that the relative error of simulated instant downward SSR flux in the PARA-C_{ad} (PARA-noC_{ad}) experiment at 76.8%, 84.8%, 88.7%, 91.6%, 93.0%, and 87.1% (59.7%, 59.9%, 65.2%, 57.4%, 56.0%, and 55.6%) grids are within ±1% at the horizontal resolution of 0.025°, 0.05°, 0.1°, 0.2°, 0.4°, and 0.8°, respectively. The clear-sky 3DSTSRE scheme with the parameterized shadow factor SFC$_p$ adjusted shows very stable good performance to simulate the downward SSR flux in different regions and time with different horizontal resolutions.

As shown in Figures 11a–11f, the regionally averaged normalized mean absolute errors (NAMEs) of the instant downward SSR flux in the PARA-noC_{ad} experiment are all above 1% and reach 3% in winter for all the resolutions. Compared to those in the PARA-noC_{ad} experiment, the regional mean NMAEs of the instant downward SSR flux in the PARA-noC_{ad} experiment largely decrease and have no significant seasonal differences for all resolutions. The regional mean NMAEs of the instant downward SSR flux in the PARA-noC_{ad} experiment are close to 0 for the resolutions of 0.1°, 0.2°, and 0.4°. Figures 11g–11l show that significant NMAEs of the instant downward SSR flux exist during the early morning and late afternoon in the PARA-noC_{ad} experiment for all resolutions. The NMAEs in the PARA-C_{ad} experiment are less than 1% throughout the day for the resolutions from 0.05° to 0.8° (Figures 11h–11l). The NMAEs in the PARA-C_{ad} experiment for the resolution of 0.025° are around
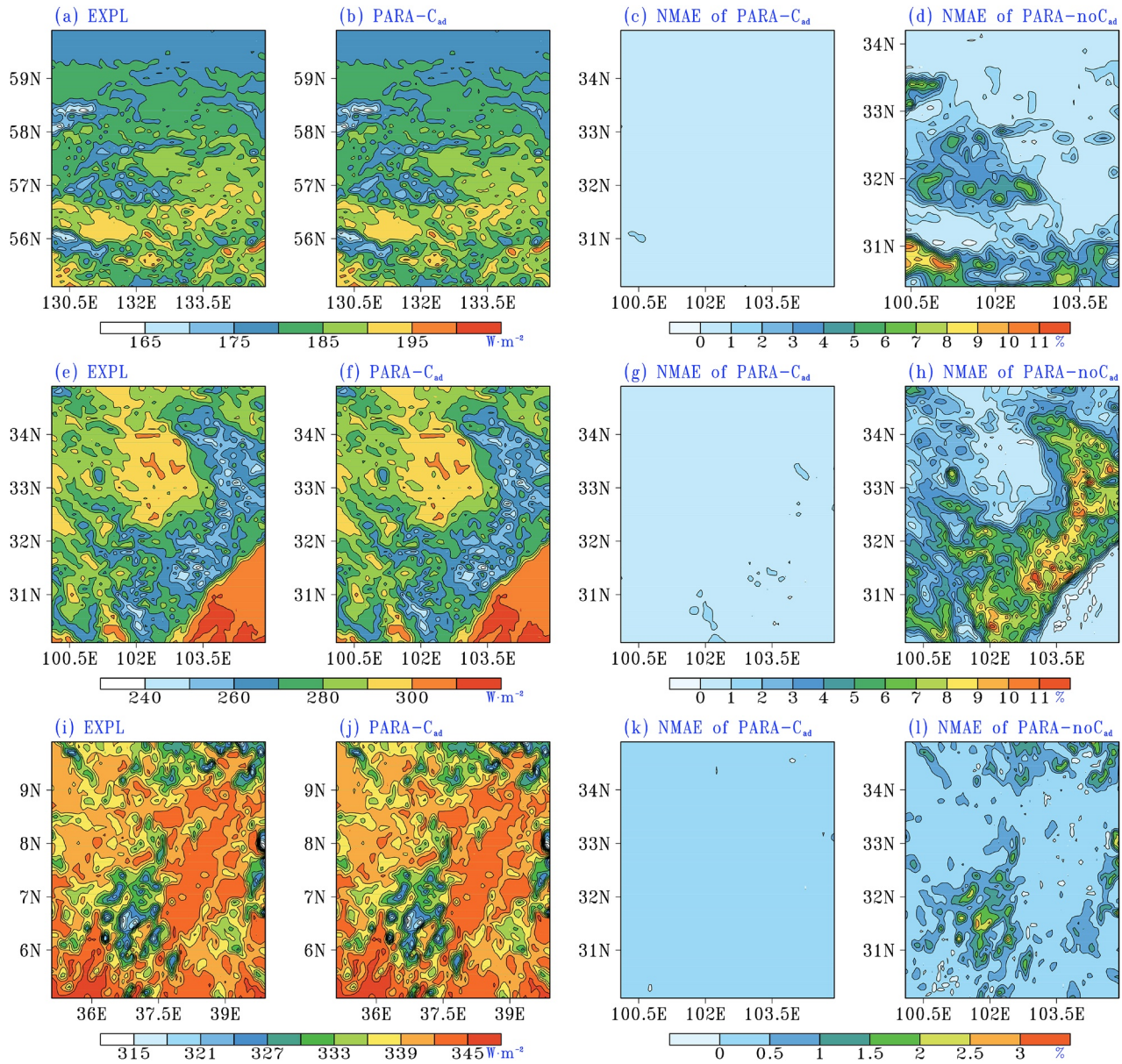
Figure 9. The annual mean downward surface solar radiation (SSR) flux at 0.1° grid resolution derived from the explicit calculations of the EXPL experiment (a, e, and i) with the resolution of 3″ and the parameterized calculations of the PARA-C_{ad} experiment (b, f, and j) over the 3 regions (Figures 2b–2d). The normalized mean absolute errors (NMAE) of downward SSR flux calculated by the PARA-C_{ad} (c, g, and k) and PARA-NoC_{ad} experiments (d, h, and l).

1% during the day and a little bit larger than those at the other resolutions. The clear-sky 3DSTSRE scheme with the adjustment factor C_{ad} still performs slightly worse in the morning (afternoon) than at noon.

Overall, from Figures 9–11, the clear-sky 3DSTSRE scheme with the parameterized shadow factor SFC_p adjusted performs well throughout the year (day) in various regions at different horizontal resolutions. In addition, the Taylor scores and correlation coefficients calculated for all the resolutions are over 0.99 at most time steps and over 0.98 at the dawn and dusk time steps (passing the 99.9% significance level), indicating the good and stable performance of the clear-sky 3DSTSRE scheme. The application of the clear-sky 3DSTSRE scheme in the 0.025° model grids still offers good descriptions of the terrain effect. Due to the requirement of enormous calculations and memory storage, it is impossible and wasteful to explicitly calculate the downward SSR flux at the sub-grids during the model integration. Obviously, the clear-sky 3DSTSRE scheme does not add additional computational
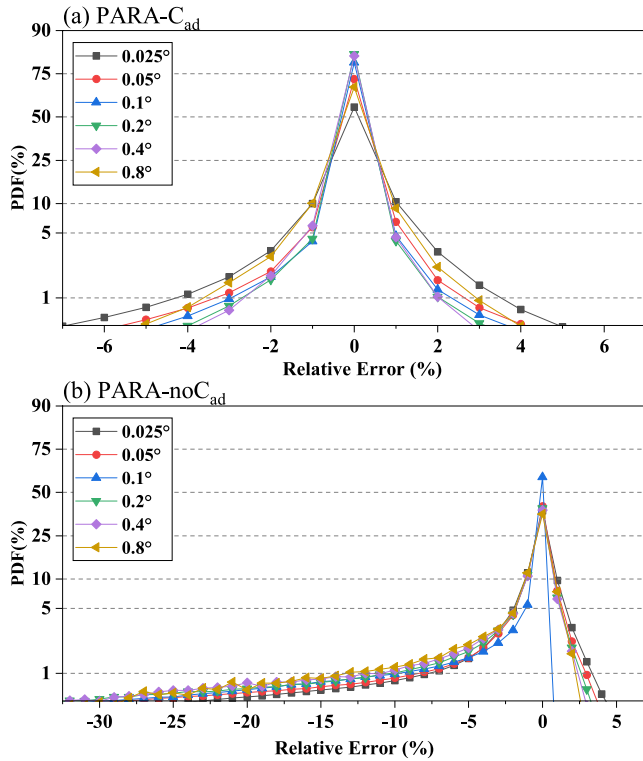
Figure 10. The probability distribution function (PDF) of relative errors in the instant downward SSR flux from the parameterized calculations of the PARA-C_{ad} experiment (a) and the PARA-noC_{ad} experiment (b) against those derived from the explicit calculations of the EXPL experiments with the resolution of 3″ over the 3 regions (Figures 2b–2d).

burden to the numerical models and achieves the equivalence of the explicitly calculated downward SSR flux at the sub-grids converted to the model grids.

5. Conclusion and Discussion

In this study, a clear-sky 3DSTSRE scheme based on the mountain radiation theory and high-resolution DEM data with full consideration of the influences of the local terrain, surrounding terrain, and surface area change has been developed and evaluated. Main conclusions are listed as follows:

The majority of calculations for the clear-sky 3DSTSRE scheme are the preparation of global terrain parameter basic data at the resolution of DEM data, including terrain slope, aspect, sky view factor, and maximal terrain elevation angle, which are used to generate the grid scale factors in the clear-sky 3DSTSRE scheme to correct the downward SSR flux calculated by the radiation scheme of plane surface. The clear-sky 3DSTSRE scheme achieves the equivalent effect of the downward SSR flux on model grids derived from those explicitly calculated on sub-grids and it can be flexibly applied to numerical models without adding additional computational burden.

The main challenge for the clear-sky 3DSTSRE scheme is to precisely represent the synergistic effects of the sub-grid terrain self and cast shadows on the direct solar radiation at surface, which is the main error source of the scheme. An adjustment parameter C_{ad} relying on the model horizontal resolutions is further used to balance the effects of the sub-grid terrain self and cast shadows. The clear-sky 3DSTSRE scheme with the parameterized shadow factor SFC_p adjusted performs well at different model horizontal resolutions over the regions featured by complex terrains.

The relative errors of the instant downward SSR flux calculated by the clear-sky 3DSTSRE scheme obey the normal distribution and are within ±1% at 76.8%, 84.8%, 88.7%, 91.6%, 93.0%, and 87.1% of the model grids with the horizontal resolution resolution of 0.025°, 0.05°, 0.1°, 0.2°, 0.4°, and 0.8°, respectively. The NMAEs of the instant downward SSR flux calculated by the clear-sky 3DSTSRE scheme are less than 1.0% (2.0%) throughout the year and the day for the grid resolutions ranging from 0.05° to 0.8° (of 0.025°). The clear-sky 3DSTSRE scheme produces Taylor scores and spatial correlation coefficients passing the 99.9% significant level for the instant downward SSR flux at different time steps and different grid resolutions. The performance of the clear-sky 3DSTSRE scheme with the shadow factor adjusted decreases slightly under the conditions with much lower solar zenith and finer model horizontal resolution. However, the spatial correlation coefficients and Taylor scores of the instant downward SSR flux in 0.025° grids produced by the clear-sky 3DSTSRE scheme with the shadow factor adjusted are above 0.98 at dawn and dusk, during which the solar zenith angle is much lower.

Overall, the clear-sky 3DSTSRE scheme with the shadow factor adjusted offers the models a detailed and precise description of the STSRE on the downward SSR flux. It has broad application prospects in various numerical models of different horizontal resolutions with the advantages of a solid physical foundation, high accuracy, minimal computational expense, strong portability and flexibility.

Due to the restriction of the calculation resources and storage space, the clear-sky 3DSTSRE scheme is evaluated in three 5° × 5° regions instead of the whole world. In addition, the study is conducted under clear-sky conditions, which idealize the impacts of atmospheric composition and ignore the influences of aerosols and clouds. To compensate for these shortcomings, the clear-sky 3DSTSRE scheme should be applied to the numerical models and validated with observations around the world in the near future.
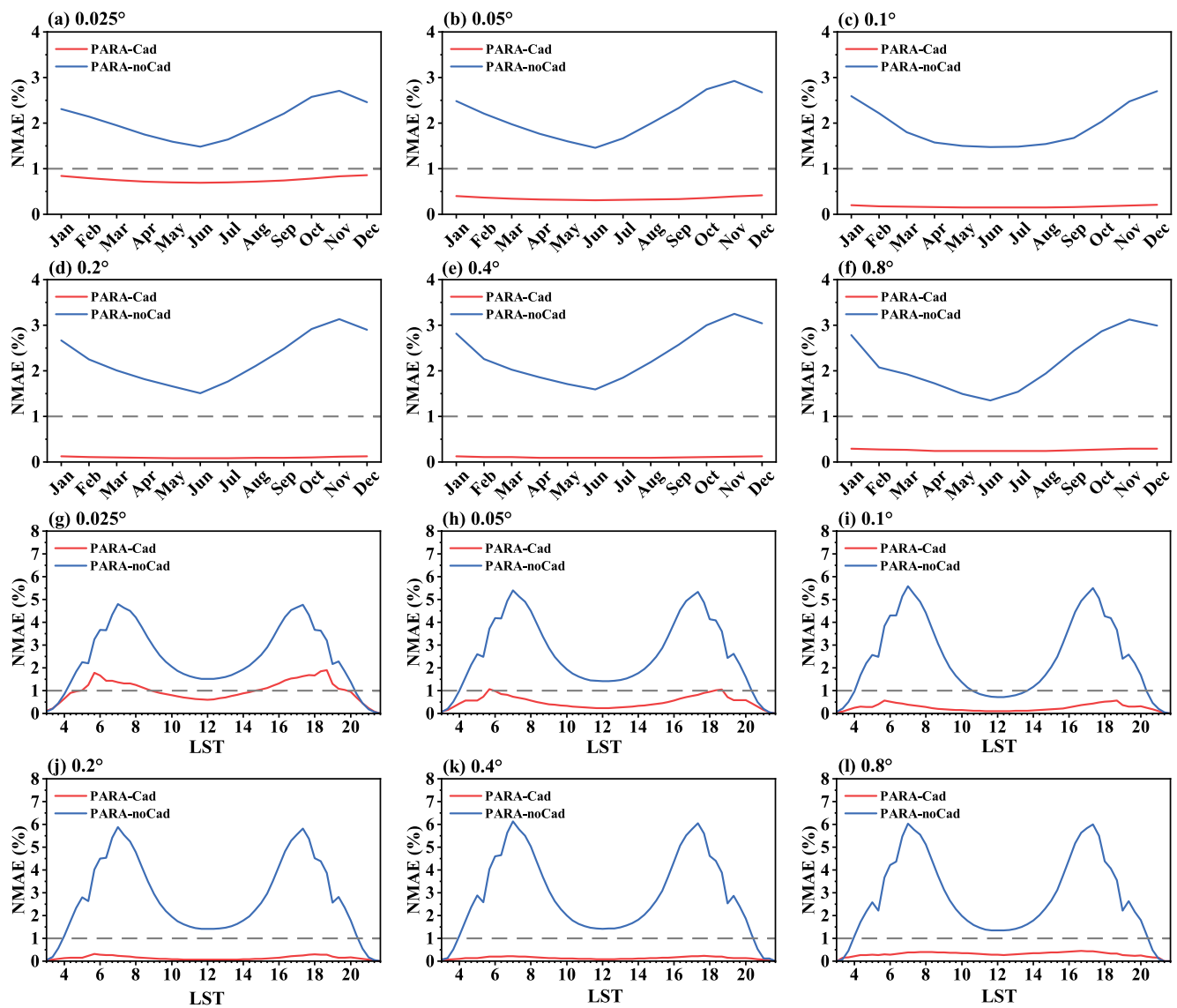
Figure 11. The regionally averaged normalized mean absolute error (NMAE) of the instant downward SSR flux from the parameterized calculations of the PARA-C$_{ad}$ experiment (red line) and the PARA-noC$_{ad}$ experiment (blue line) with different grid resolutions against those derived from the explicit calculations of the EXPL experiments with the resolution of 3″ over the 3 regions (Figures 2b–2d) (a–f) for each month (g–l) for local solar time of a day.

Data Availability Statement

References

Adobe. (2018). Adobe illustrator CC 2018 [software]. Adobe. Retrieved from https://www.adobe.com/products/illustrator.html

Aguilar, C., Herrero, J., & Polo, M. (2010). Topographic effects on solar radiation distribution in mountainous watersheds and their influence on reference evapotranspiration estimates at watershed scale. *Hydrology and Earth System Sciences*, *14*(12), 2479–2494. https://doi.org/10.5194/hess-14-2479-2010

Arnold, N. S., Rees, W. G., Hodson, A. J., & Kohler, J. (2006). Topographic controls on the surface energy balance of a high Arctic valley glacier. *Journal of Geophysical Research*, *111*(F2), F02011. https://doi.org/10.1029/2005jf000426

Arthur, R. S., Lundquist, K. A., Mirocha, J. D., & Chow, F. K. (2018). Topographic effects on radiation in the WRF model with the immersed boundary method: Implementation, validation, and application to complex terrain. *Monthly Weather Review*, *146*(10), 3277–3292. https://doi.org/10.1175/mwr-d-18-0108.1

Barry, R. G. (2008). *Mountain weather and climate* (3rd edn). Cambridge University Press. https://doi.org/10.1017/CBO9780511754753

Carvalho, D., Rocha, A., Gómez-Gesteira, M., & Santos, C. (2012). A sensitivity study of the WRF model in wind simulation for an area of high wind energy. *Environmental Modelling & Software*, *33*, 23–34. https://doi.org/10.1016/j.envsoft.2012.01.019

Chen, Y., Hall, A., & Liou, K. N. (2006). Application of three-dimensional solar radiative transfer to mountains. *Journal of Geophysical Research*, *111*(D21), 1–13. https://doi.org/10.1029/2006JD007163

COLA. (2017). The grid analysis and Display system (GrADS) [software]. *Center for ocean-land-atmosphere studies (COLA)*. George Mason University. Retrieved from ftp://cola.gmu.edu/grads/2.2/grads-2.2.0-src.tar.gz

Corripio, J. G. (2003). Vectorial algebra algorithms for calculating terrain parameters from DEMs and solar radiation modelling in mountainous terrain. *International Journal of Geographical Information Science*, *17*(1), 1–23. https://doi.org/10.1080/713811744

Davies, L. A., & Brown, A. R. (2001). Assessment of which scales of orography can be credibly resolved in a numerical model. *Quarterly Journal of the Royal Meteorological Society*, *127*(574), 1225–1237. https://doi.org/10.1256/smsqj.57404

Dozier, J., & Frew, J. (1990). Rapid calculation of terrain parameters for radiation modeling from digital elevation data. *IEEE Transactions on Geoscience and Remote Sensing*, *28*(5), 963–969. https://doi.org/10.1109/36.58986

Dubayah, R., & Loechel, S. (1997). Modeling topographic solar radiation using GOES data. *Journal of Applied Meteorology*, *36*(2), 141–154. https://doi.org/10.1175/1520-0450(1997)036<0141:Mtsrug>2.0.Co;2

Dubayah, R. C. (1994). Modeling a solar radiation topoclimatology for the rio grande river basin. *Journal of Vegetation Science*, *5*(5), 627–640. https://doi.org/10.2307/3235879

Elvidge, A. D., Sandu, I., Wedi, N., Vosper, S. B., Zadra, A., Boussetta, S., et al. (2019). Uncertainty in the representation of orography in weather and climate models and implications for parameterized drag. *Journal of Advances in Modeling Earth Systems*, *11*(8), 2567–2585. https://doi.org/10.1029/2019MS001661

Essery, R., & Marks, D. (2007). Scaling and parametrization of clear-sky solar radiation over complex topography. *Journal of Geophysical Research*, *112*(D10). D10122. https://doi.org/10.1029/2006JD007650

Falasca, S., & Curci, G. (2018). High-resolution air quality modeling: Sensitivity tests to horizontal resolution and urban canopy with WRF-CHIMERE. *Atmospheric Environment*, *187*, 241–254. https://doi.org/10.1016/j.atmosenv.2018.05.048

Feng, L., & Zhang, Y. (2007). Impacts of the thermal effects of sub-grid orography on the heavy rainfall events along the Yangtze River Valley in 1991. *Advances in Atmospheric Sciences*, *24*(5), 881–892. https://doi.org/10.1007/s00376-007-0881-4

Frey, H., & Paul, F. (2012). On the suitability of the SRTM DEM and ASTER GDEM for the compilation of topographic parameters in glacier inventories. *International Journal of Applied Earth Observation and Geoinformation*, *18*, 480–490. https://doi.org/10.1016/j.jag.2011.09.020

Fu, P., & Rich, P. M. (1999). Design and implementation of the Solar Analyst: An ArcView extension for modeling solar radiation at landscape scales. In *Paper presented at the Proceedings of the nineteenth annual ESRI user conference*.

Fujisada, H., Urai, M., & Iwasaki, A. (2012). Technical methodology for ASTER global DEM. *IEEE Transactions on Geoscience and Remote Sensing*, *50*(10), 3725–3736. https://doi.org/10.1109/TGRS.2012.2187300

GNU. (2015). The GNU Fortran compiler [software]. GNU, Free Software Foundation, Inc. Retrieved from https://gcc.gnu.org/wiki/GFortranSource

Gorokhovich, Y., & Voustianiouk, A. (2006). Accuracy assessment of the processed SRTM-based elevation data by CGIAR using field data from USA and Thailand and its relation to the terrain characteristics. *Remote Sensing of Environment*, *104*(4), 409–415. https://doi.org/10.1016/j.rse.2006.05.012

Gu, C., Huang, A., Wu, Y., Yang, B., Mu, X., Zhang, X., & Cai, S. (2020). Effects of subgrid terrain radiative forcing on the ability of RegCM4.1 in the simulation of summer precipitation over China. *Journal of Geophysical Research: Atmospheres*, *125*(12), e2019JD032215. https://doi.org/10.1029/2019JD032215

Gu, Y., Liou, K. N., Lee, W. L., & Leung, L. R. (2012). Simulating 3-D radiative transfer effects over the Sierra Nevada Mountains using WRF. *Atmospheric Chemistry and Physics*, *12*(20), 9965–9976. https://doi.org/10.5194/acp-12-9965-2012

Han, F. Q., Miao, J. F., & Wang, Y. H. (2018). Impact of radiation parameterization of topographic effects on sea breeze circulation and cloud water pattern over the Hainan Island. *Journal of Tropical Meteorology*, *34*(1), 115–132. (in Chinese).

Hao, D., Bisht, G., Gu, Y., Lee, W. L., Liou, K. N., & Leung, L. R. (2021). A parameterization of sub-grid topographical effects on solar radiation in the E3SM land model (version 1.0): Implementation and evaluation over the Tibetan plateau. *Geoscientific Model Development*, *14*(10), 6273–6289. https://doi.org/10.5194/gmd-14-6273-2021

Hauge, G., & Hole, L. R. (2003). Implementation of slope irradiance in Mesoscale Model version 5 and its effect on temperature and wind fields during the breakup of a temperature inversion. *Journal of Geophysical Research*, *108*(D2), 4058. https://doi.org/10.1029/2002jd002575

He, S., Smirnova, T. G., & Benjamin, S. G. (2019). A scale-aware parameterization for estimating subgrid variability of downward solar radiation using high-resolution digital elevation model data. *Journal of Geophysical Research: Atmospheres*, *124*(24), 13680–13692. https://doi.org/10.1029/2019jd031563

Helbig, N., & Lowe, H. (2012). Shortwave radiation parameterization scheme for subgrid topography. *Journal of Geophysical Research: Atmospheres*, *117*(D3), D03112. https://doi.org/10.1029/2011jd016465

Helbig, N., Löwe, H., & Lehning, M. (2009). Radiosity approach for the shortwave surface radiation balance in complex terrain. *Journal of the Atmospheric Sciences*, *66*(9), 2900–2912. https://doi.org/10.1175/2009jas2940.1

Helbig, N., Löwe, H., Mayer, B., & Lehning, M. (2010). Explicit validation of a surface shortwave radiation balance model over snow-covered complex terrain. *Journal of Geophysical Research*, *115*(D18), D18113. https://doi.org/10.1029/2010jd013970

Hock, R., & Holmgren, B. (2005). A distributed surface energy-balance model for complex topography and its application to storglaciären, Sweden. *Journal of Glaciology*, *51*(172), 25–36. https://doi.org/10.3189/172756505781829566

Hua, S., Xu, X., & Chen, B. (2020). Influence of multiscale orography on the initiation and maintenance of a precipitating convective system in north China: A case study. *Journal of Geophysical Research: Atmospheres*, *125*(13). https://doi.org/10.1029/2019JD031731

Huang, D. Q., & Qian, Y. F. (2008). The effects of the slope irradiance on different weather processes under different model resolutions. *Acta Meteorologica Sinica*, *66*(1), 90–100. (in Chinese). https://doi.org/10.11676/qxxb2008.009

Jarvis, A., Reuter, H. I., Nelson, A., & Guevara, E. (2008). The Shuttle radar topography mission (SRTM) 90m digital elevation Database v4.1 [Dataset]. International Centre for Tropical Agriculture (CIAT). Retrieved from https://developers.google.com/earth-engine/datasets/catalog/CGIAR_SRTM90_V4

Ji, Z., & Kang, S. (2013). Double-nested dynamical downscaling experiments over the Tibetan plateau and their projection of climate change under two RCP scenarios. *Journal of the Atmospheric Sciences*, *70*(4), 1278–1290. https://doi.org/10.1175/JAS-D-12-0155.1

Jiménez, P. A., & Dudhia, J. (2012). Improving the representation of resolved and unresolved topographic effects on surface wind in the WRF model. *Journal of Applied Meteorology and Climatology*, *51*(2), 300–316. https://doi.org/10.1175/jamc-d-11-084.1

Kalogirou, S. A. (2014). Chapter 2 - environmental characteristics. In S. A. Kalogirou (Ed.), *Solar energy engineering* (2nd ed., pp. 51–123). Academic Press. https://doi.org/10.1016/B978-0-12-397270-5.00002-9

Keith, F., & Kreider, J. F. (1978). *Principles of solar engineering* (1st ed.). McGraw-Hill.

Kittler, R., & Darula, S. (2013). Determination of time and sun position system. *Solar Energy*, *93*, 72–79. https://doi.org/10.1016/j.solener.2013.03.021

Kondrat'yev, K. Y. (1965). *Radiative heat exchange in the atmosphere (translated from the Russian by O. Tedder)* (p. 332). Pergamon Press. https://doi.org/10.1016/C2013-0-05325-X

Krieger, G., Moreira, A., Fiedler, H., Hajnsek, I., Werner, M., Younis, M., & Zink, M. (2007). TanDEM-X: A satellite formation for high-resolution SAR interferometry. *IEEE Transactions on Geoscience and Remote Sensing*, *45*(11), 3317–3341. https://doi.org/10.1109/TGRS.2007.900693

Lalande, M., Ménégoz, M., Krinner, G., Naegeli, K., & Wunderle, S. (2021). Climate change in the high mountain Asia in CMIP6. *Earth System Dynamics*, *12*(4), 1061–1098. https://doi.org/10.5194/esd-12-1061-2021

Lee, W.-L., Gu, Y., Liou, K. N., Leung, L. R., & Hsu, H.-H. (2015). A global model simulation for 3-D radiative transfer impact on surface hydrology over the Sierra Nevada and Rocky Mountains. *Atmospheric Chemistry and Physics*, *15*(10), 5405–5413. https://doi.org/10.5194/acp-15-5405-2015

Lee, W.-L., Liou, K. N., & Hall, A. (2011). Parameterization of solar fluxes over mountain surfaces for application to climate models. *Journal of Geophysical Research*, *116*(D1), D01101. https://doi.org/10.1029/2010jd014722

Lee, W.-L., Liou, K. N., & Wang, C.-C. (2013). Impact of 3-D topography on surface radiation budget over the Tibetan Plateau. *Theoretical and Applied Climatology*, *113*(1), 95–103. https://doi.org/10.1007/s00704-012-0767-y

Lee, W.-L., Liou, K.-N., Wang, C.-C., Gu, Y., Hsu, H.-H., & Li, J.-L. F. (2019). Impact of 3-D radiation-topography interactions on surface temperature and energy budget over the Tibetan plateau in winter. *Journal of Geophysical Research: Atmospheres*, *124*(3), 1537–1549. https://doi.org/10.1029/2018JD029592

Li, J., & Luo, J. (2015). Estimation of solar radiation over rugged terrains based on clear sky condition. *Arid Land Geography*, *38*(1), 120–127. (in Chinese with English abstract).

Li, P., Furtado, K., Zhou, T., Chen, H., & Li, J. (2021). Convection-permitting modelling improves simulated precipitation over the central and eastern Tibetan Plateau. *Quarterly Journal of the Royal Meteorological Society*, *147*(734), 341–362. https://doi.org/10.1002/qj.3921

Li, X., Koike, T., & Cheng, G. (2002). Retrieval of snow reflectance from Landsat data in rugged terrain. *Annals of Glaciology*, *34*, 31–37. https://doi.org/10.3189/172756402781817635

Liou, K. N., Gu, Y., Leung, L. R., Lee, W. L., & Fovell, R. G. (2013). A WRF simulation of the impact of 3-D radiative transfer on surface hydrology over the Rocky Mountains and Sierra Nevada. *Atmospheric Chemistry and Physics*, *13*(23), 11709–11721. https://doi.org/10.5194/acp-13-11709-2013

Liou, K. N., Lee, W.-L., & Hall, A. (2007). Radiative transfer in mountains: Application to the Tibetan plateau. *Geophysical Research Letters*, *34*(23). L23809. https://doi.org/10.1029/2007gl031762

Liu, B. Y. H., & Jordan, R. C. (1960). The interrelationship and characteristic distribution of direct, diffuse and total solar radiation. *Solar Energy*, *4*(3), 1–19. https://doi.org/10.1016/0038-092X(60)90062-1

Manners, J., Vosper, S. B., & Roberts, N. (2012). Radiative transfer over resolved topographic features for high-resolution weather prediction. *Quarterly Journal of the Royal Meteorological Society*, *138*(664), 720–733. https://doi.org/10.1002/qj.956

Mass, C. F., Ovens, D., Westrick, K., & Colle, B. A. (2002). Dose increasing horizontal resolution produce more skillful forecast?: The results of two years of real-time numerical weather prediction over the Pacific northwest. *Bulletin of the American Meteorological Society*, *83*(3), 407–430. https://doi.org/10.1175/1520-0477(2002)083<0407:Dihrpm>2.3.Co;2

Maurya, R. K. S., Sinha, P., Mohanty, M. R., & Mohanty, U. C. (2018). RegCM4 model sensitivity to horizontal resolution and domain size in simulating the Indian summer monsoon. *Atmospheric Research*, *210*, 15–33. https://doi.org/10.1016/j.atmosres.2018.04.010

Müller, M. D., & Scherer, D. (2005). A grid- and subgrid-scale radiation parameterization of topographic effects for mesoscale weather forecast models. *Monthly Weather Review*, *133*(6), 1431–1442. https://doi.org/10.1175/mwr2927.1

Niu, X., Tang, J., Chen, D., Wang, S., & Ou, T. (2021). Elevation-dependent warming over the Tibetan plateau from an ensemble of CORDEX-EA regional climate simulations. *Journal of Geophysical Research: Atmospheres*, *126*(9), e2020JD033997. https://doi.org/10.1029/2020JD033997

Oliphant, A. J., Spronken-Smith, R. A., Sturman, A. P., & Owens, I. F. (2003). Spatial variability of surface radiation fluxes in mountainous terrain. *Journal of Applied Meteorology*, *42*(1), 113–128. https://doi.org/10.1175/1520-0450(2003)042<0113:Svosrf>2.0.Co;2

Olson, M., & Rupper, S. (2019). Impacts of topographic shading on direct solar radiation for valley glaciers in complex topography. *The Cryosphere*, *13*(1), 29–40. https://doi.org/10.5194/tc-13-29-2019

Olyphant, G. A. (1984). Insolation topoclimates and potential ablation in alpine snow accumulation basins: Front range, Colorado. *Water Resources Research*, *20*(4), 491–498. https://doi.org/10.1029/WR020i004p00491

OriginLab. (2021). OriginPro 2021b [software]. OriginLab. Retrieved from https://store.originlab.com/store/Default.aspx?CategoryID=0

Phillips, N. A. (1957). A coordinate system having some special advantages for numerical forecasting. *Journal of Meteorology*, *14*(2), 184–185. https://doi.org/10.1175/1520-0469(1957)014<0184:Acshss>2.0.Co;2

Reuter, H. I., Nelson, A., & Jarvis, A. (2007). An evaluation of void-filling interpolation methods for SRTM data. *International Journal of Geographical Information Science*, *21*(9), 983–1008. https://doi.org/10.1080/13658810601169899

Rodriguez, E., Morris, C. S., & Belz, J. E. (2006). A global assessment of the SRTM performance. *Photogrammetric Engineering & Remote Sensing*, *72*(3), 249–260. https://doi.org/10.14358/PERS.72.3.249

Ruiz-Arias, J. A., Cebecauer, T., Tovar-Pescador, J., & Šúri, M. (2010). Spatial disaggregation of satellite-derived irradiance using a high-resolution digital elevation model. *Solar Energy*, *84*(9), 1644–1657. https://doi.org/10.1016/j.solener.2010.06.002

Ruiz-Arias, J. A., Pozo-Vázquez, D., Lara-Fanego, V., Santos-Alamillos, F. J., & Tovar-Pescador, J. (2011). A high-resolution topographic correction method for clear-sky solar irradiance derived with a numerical weather prediction model. *Journal of Applied Meteorology and Climatology*, *50*(12), 2460–2472. https://doi.org/10.1175/2011JAMC2571.1

Sandu, I., van Niekerk, A., Shepherd, T. G., Vosper, S. B., Zadra, A., Bacmeister, J., et al. (2019). Impacts of orography on large-scale atmospheric circulation. *npj Climate and Atmospheric Science*, *2*(1), 10. https://doi.org/10.1038/s41612-019-0065-9

Schaaf, C., & Wang, Z. (2015). The moderate resolution imaging spectroradiometer (MODIS) MCD43A3 version 6 albedo model dataset [dataset]. NASA EOSDIS Land Processes DAAC. https://e4ftl01.cr.usgs.gov/MOTA/MCD43A3.006/

Senkova, A. V., Rontu, L., & Savijarvi, H. (2007). Parametrization of orographic effects on surface radiation in HIRLAM. *Tellus A*, *59*(3), 279–291. https://doi.org/10.1111/j.1600-0870.2007.00235.x

Sharpnack, D. A., & Akin, G. (1969). An algorithm for computing slope and aspect from elevations. *Photogrammetric Engineering*, *35*(3), 247–248.

Shen, Y. F., & Hu, J. L. (2006). Slope irradiance scheme in GRAPES and its effect on simulation of short range weather processes. *Chinese Journal of Atmospheric Sciences*, *30*(6), 1129–1137. (in Chinese). https://doi.org/10.3878/j.issn.1006-9895.2006.06.07

Skidmore, A. K. (1989). A comparison of techniques for calculating gradient and aspect from a gridded digital elevation model. *International Journal of Geographical Information Systems*, *3*(4), 323–334. https://doi.org/10.1080/02693798908941519

Sreedevi, P., Sreekanth, P., Khan, H., & Ahmed, S. (2013). Drainage morphometry and its influence on hydrology in a semi arid region: Using SRTM data and GIS. *Environmental Earth Sciences*, *70*(2), 839–848. https://doi.org/10.1007/s12665-012-2172-3

Takaku, J., Tadono, T., & Tsutsui, K. (2014). Generation of high resolution global DSM from ALOS PRISM. *ISPRS - International Archives of the Photogrammetry, Remote Sensing and Spatial Information Sciences*, 243–248. XL-4. https://doi.org/10.5194/isprsarchives-XL-4-243-2014

Taylor, K. E. (2001). Summarizing multiple aspects of model performance in a single diagram. *Journal of Geophysical Research*, *106*(D7), 7183–7192. https://doi.org/10.1029/2000JD900719

Tovar-Pescador, J., Pozo-Vazquez, D., Ruiz-Arias, J., Batlles, J., López, G., & Bosch, J. (2006). On the use of the digital elevation model to estimate the solar radiation in areas of complex topography. *Meteorological Applications*, *13*(3), 279–287. https://doi.org/10.1017/S1350482706002258

van Niekerk, A., Sandu, I., Zadra, A., Bazile, E., Kanehama, T., Köhler, M., et al. (2020). COnstraining ORographic drag effects (COORDE): A model comparison of resolved and parametrized orographic drag. *Journal of Advances in Modeling Earth Systems*, *12*(11), e2020MS002160. https://doi.org/10.1029/2020MS002160

Vician, P., Palacka, M., Ďurčanský, P., & Jandačka, J. (2017). Determination of optimal position of solar trough collector. *Procedia Engineering*, *192*, 941–946. https://doi.org/10.1016/j.proeng.2017.06.162

Vosper, S. B., Niekerk, A., Elvidge, A., Sandu, I., & Beljaars, A. (2020). What can we learn about orographic drag parametrisation from high-resolution models? A case study over the rocky mountains. *Quarterly Journal of the Royal Meteorological Society*, *146*(727), 979–995. https://doi.org/10.1002/qj.3720

Wallace, J. M., Tibaldi, S., & Simmons, A. J. (1983). Reduction of systematic forecast errors in the ECMWF model through the introduction of an envelope orography. *Quarterly Journal of the Royal Meteorological Society*, *109*(462), 683–717. https://doi.org/10.1002/qj.49710946202

Wang, S., Chen, W., & Cihlar, J. (2002). New calculation methods of diurnal distribution of solar radiation and its interception by canopy over complex terrain. *Ecological Modelling*, *155*(2), 191–204. https://doi.org/10.1016/S0304-3800(02)00122-9

Wang, Y., Yang, K., Zhou, X., Chen, D. L., Lu, H., Ouyang, L., et al. (2020). Synergy of orographic drag parameterization and high resolution greatly reduces biases of WRF-simulated precipitation in central Himalaya. *Climate Dynamics*, *54*(3–4), 1729–1740. https://doi.org/10.1007/s00382-019-05080-w

Williams, L. F. (1976). A modification to the half-interval search (binary search) method. In *Proceedings of the 14th annual Southeast regional conference*. Paper presented at the. https://doi.org/10.1145/503561.503582

Wu, G. X., He, B., Duan, A. M., Liu, Y. M., & Yu, W. (2017). Formation and variation of the atmospheric heat source over the Tibetan Plateau and its climate effects. *Advances in Atmospheric Sciences*, *34*(10), 1169–1184. https://doi.org/10.1007/s00376-017-7014-5

Xu, X., Xue, M., Teixeira, M. A., Tang, J., & Wang, Y. (2019). Parameterization of directional absorption of orographic gravity waves and its impact on the atmospheric general circulation simulated by the weather Research and forecasting model. *Journal of the Atmospheric Sciences*, *76*(11), 3435–3453. https://doi.org/10.1175/jas-d-18-0365.1

Yan, G., Chu, Q., Tong, Y., Mu, X., Qi, J., Zhou, Y., et al. (2021). An operational method for validating the downward shortwave radiation over rugged terrains. *IEEE Transactions on Geoscience and Remote Sensing*, *59*(1), 714–731. https://doi.org/10.1109/TGRS.2020.2994384

Yu, R., Zhang, Y., Wang, J., Li, J., Chen, H., Gong, J., & Chen, J. (2019). Recent progress in numerical atmospheric modeling in China. *Advances in Atmospheric Sciences*, *36*(9), 938–960. https://doi.org/10.1007/s00376-019-8203-1

Zhang, X., Huang, A., Dai, Y., Li, W., Gu, C., Yuan, H., et al. (2022). Influences of 3D sub-grid terrain radiative effect on the performance of CoLM over heihe river basin, Tibetan plateau. *Journal of Advances in Modeling Earth Systems*, *14*(1), e2021MS002654. https://doi.org/10.1029/2021ms002654

Zhang, Y., Huang, A., & Zhu, X. (2006). Parameterization of the thermal impacts of sub-grid orography on numerical modeling of the surface energy budget over East Asia. *Theoretical and Applied Climatology*, *86*(1–4), 201–214. https://doi.org/10.1007/s00704-005-0209-1

Zhang, Z. Q., Zhou, X. J., & Li, W. L. (2002). Preliminary Numerical study of topographic effects of the Tibetan Plateau on surface direct radiation. *Acta Meteorologica Sinica*, *16*(1), 50–61.

Zhou, X., Yang, K., Beljaars, A., Li, H., Lin, C., Huang, B., & Wang, Y. (2019). Dynamical impact of parameterized turbulent orographic form drag on the simulation of winter precipitation over the Western Tibetan Plateau. *Climate Dynamics*, *53*(1–2), 707–720. https://doi.org/10.1007/s00382-019-04628-0

Zhu, Y.-Y., & Yang, S. (2020). Evaluation of CMIP6 for historical temperature and precipitation over the Tibetan Plateau and its comparison with CMIP5. *Advances in Climate Change Research*, *11*(3), 239–251. https://doi.org/10.1016/j.accre.2020.08.001